M.Sc. Dissertation

Framework for semi-automated object-based image classification of invasive alien plant species in South Africa: *Harrisia pomanensis* as a case study

by

Madodomzi Mafanya

Supervisor: Mr. Philemon Tsele

Co-Supervisor: Dr. Joel Botai

Submitted in partial fulfilment of the requirements for the degree

Master of Science in Geoinformatics.

In the Faculty of Natural & Agricultural Sciences

University of Pretoria

December 2018

Declaration of originality

I, Madodomzi Mafanya declare that the dissertation, which I hereby submit for degree MSc Geoinformatics at the University of Pretoria, is my own work and has not previously been submitted by me for a degree at this or any other tertiary institution.

SIGNATURE:……..

DATE: …….

ACKNOWLEDGEMENTS

This research work was supported by the South African National Department of Environmental Affairs through its funding of the South African National Biodiversity Institute: Invasive Species Programme (SANBI:ISP), project number P038. Special thanks go to my mentor and academic supervisor, Mr PL Tsele for the consistent tireless effort that he put to help me prepare this dissertation and its preceding manuscripts. Without him, submission of this research work would not have been possible. Moreover, I would like to thank my co-supervisors, Dr OJ Botai and Mr P Manyama for leading this work since its conception. I am also expressing my gratitude to the founding director of CAD Mapping Aerial Surveyors, Mr DJ Cochran for providing equipment and additional financial support to fund this project. I would also like to thank Misters Barend Swart, Thabang Monate, Phomolo Seriba, Owen Vyk, Monty Tshwale, Malherbe Rossouw, Sedgely Pinneken, Eric Economon and Dr G Chirima for assisting with the recording of spectral data, GPS data and image data acquisition as well as their help on data processing. I thank Faizel Khan for helping with the radiometric calibration accuracy assessment. I am further extending my appreciation to my mother and my father as well as my siblings Mphumzi, Nokuthula, Khayelihle and Siphesihle Mafanya for their continued encouragement throughout the duration of the MSc programme. I am grateful for the boundless help and support that I have received from my special friend Aphiwe Mjiwu during the course of my studies. This contribution is dedicated to my nieces (Sinovuyo, Okuhle, Elihle and Zimi), my nephews (Ntsika, Lindokuhle and Junior) and my daughter and my son, Indiphile and Alandile Mafanya, respectively.

PUBLICATION MATERIAL FROM THIS DISSERTATION

1. Mafanya, M.; Tsele, P.; Botai, J.; Manyama, P.; Swart, B.; Monate, T. Evaluating pixel and object based image classification techniques for mapping plant invasions from UAV derived aerial imagery: *Harrisia pomanensis* as a case study. ISPRS Journal of Photogrammetry and Remote Sensing.2017, 129:1-11. https://doi.org/10.1016/j.isprsjprs.2017.04.009

2. Mafanya, M.; Tsele, P.; Botai, O. J.; Manyama, P.; Chirima, G.J.; Monate, T. Radiometric calibration framework for ultra-high resolution UAV derived orthomosaics for large scale mapping of invasive alien plants in semi-arid woodlands: *Harrisia pomanensis* as a case study. Unmanned Aerial Systems (UAS) for environmental applications special issue. International Journal of Remote Sensing. 39(15-16):5119-5140.
   DOI: 10.1080/01431161.2018.1490503

   Preliminary results of the radiometric calibration framework were presented at the 37th International Symposium on Remote Sensing of Environment (ISRSE-37) that took place from 8 to 12 May 2017.

Madodomzi Mafanya was the responsible author in the manuscripts listed above. These research articles involved various co-authors who contributed by reviewing the whole papers before they were submitted for publication. These manuscripts provide details on the methodology and results of this framework.

ABSTRACT

Invasive alien plants (IAPs) not only pose a serious threat to biodiversity and water resources but also have impacts on human and animal wellbeing. An important step in IAPs management is to map their location as there is a strong correlation between the spatial extent of an invaded area and the effort required for clearing the plant invasion. However, the traditional GPS based IAPs mapping field campaigns are costly, time consuming and labour intensive. The developments in the Unmanned Aerial Vehicle (UAV) technology have afforded the remote sensing (RS) community the opportunity to map IAPs at enhanced temporal and spatial resolutions. As a result, this framework synthesises a UAV-RS approach for mapping invasive alien plants in South African semi-arid woodlands using *Harrisia pomanensis* (the Midnight lady) as a case study. In particular, this framework outlines procedures for geometric and radiometric calibration of UAV-derived orthomosaics as well a semi-automated object-based image classification technique for mapping IAPs. The geometric calibration was conducted in the Agisoft Lens software package to determine the camera interior orientation parameters. Since sample photos of the LCD screen were taken from a short-range, there were more radial than tangential distortions. In addition, a scene illumination uniformity statistical inference allowed for the radiometric calibration of the entire scene using parameters derived from radiometric calibration targets placed only in one spot within the study area using the empirical line method (ELM). In particular, accuracy assessment of the radiometric calibration resulted in a correlation coefficient (*r*) value of 0.977 between *in situ* measured reflectance and the reflectance values derived from the calibrated image wavebands. This strong correlation validated the proposed UAV-RS ELM based radiometric calibration method for applications in semi-arid woodlands. Furthermore, out of the five evaluated image classifiers, the case study demonstrated that the object-based supervised *Bhattacharya* classifier which gave 90% and 95.7% producer and user accuracies, respectively, produced more accurate results for mapping *Harrisia pomanensis*. Even more so, an area based accuracy assessment showed that the *Bhattacharya* classifier mapped *Harrisia pomanensis* better than the *Maxver* classifier (i.e. the second best algorithm) with mapping accuracy averages of 86.1% and 65.2%, respectively, for all the different polygon area sizes. Future research should ascertain whethe radiometric calibration increases mapping accuracy in large scale (>100ha) UAV-RS applications.

TABLE OF CONTENTS

LIST OF FIGURES

LIST OF TABLES

CHAPTER 1

1. Introduction

1.1. General introduction

Invasive alien plants (IAPs) not only pose a serious threat to biodiversity and water resources but also have impacts on human and animal wellbeing (Poona and Shezi, 2010). The IAPs alter the functioning of ecosystems by degrading the land, diminishing native flora, reducing farming and grazing potential, and/or by changing soil dynamics and ecosystem fire regimes (Richardson and van Wilgen, 2004; Van Wilgen, 2009; Vilà et al., 2011). It is estimated that about 10.1 million hectares of land is invaded by IAPs in South Africa (Kandeh et al., 2001). Moreover, it is estimated that IAPs reduce total catchments runoff by 1 444 million m^3 in the country (Le Maitre et al., 2013). The IAPs also displace economically important native flora. The IAPs cost South Africans tens of billions rands annually as a result of lost agricultural productivity and the IAP monitoring or management expenditure (SANBI, 2018). Cactus plants, in particular, do not consume a lot of water compared to other IAPs but are generally unpalatable to most important South African herbivores and therefore their land invasion reduces grazing potential (Richardson and van Wilgen, 2004). In addition, cacti notably reduce grazing potential by replacing pasture or making it unpleasant to grazing animals (DAF, 2013). On the other hand, in some localities, cacti displace flowers that can be harvested for their economic value (Richardson and van Wilgen, 2004).

An important step in IAPs management is to map their location (Evangelista et al., 2009; Clout and Williams, 2009). Accurate spatial estimates are crucial because there is a strong correlation between the spatial extent of an invaded area and the effort required for clearing the plant invasion (Wilson et al., 2013). Spatial data is important in the process of generating simulation models for monitoring control programmes, assessing invasion risk and modelling eradication feasibility (Fox et al., 2013). Timely mapping and rapid delimitation of the spatial extent of the IAPs can facilitate decision making regarding the feasibility and effectiveness of eradication and/or containment (Fox et al., 2013). Remote sensing has the potential to support the use of remotely-sensed imagery for locating, mapping and managing IAPs (Müllerová et al., 2013).

There are two main optical remote sensing approaches for mapping and monitoring IAPs, namely, high spectral resolution with low spatial resolution and high spatial resolution with low spectral resolution (Underwood et al., 2003). The high spectral resolution approach

entails the use of hyperspectral sensors for collecting hundreds of narrow bands (less than 10 nm bandwidth) in the visible, near infrared and shortwave infrared regions of the electromagnetic spectrum (Huang and Asner, 2009). On the other hand, the high spatial resolution approach usually makes use of spaceborne and/or airborne multispectral imagery as well as aerial photography. The developments in Unmanned Aerial Vehicle (UAV) technology have afforded the remote sensing community the opportunity to map the environment at enhanced spatial resolutions. Utility of consumer grade digital cameras (CGDC) with very high spatial but low spectral resolution in UAV remote sensing (UAV-RS) is often made due to the limited payload capacity on these systems (<5 kg) (Laliberte et al., 2011). The high spatial resolution can be attributed to the fact that UAV systems allow for data acquisition at low flight altitudes of usually less than 200m above ground level (AGL) depending on global and country specific aviation rules (Cracknell, 2017). In particular, orthomosaics derived from CGDCs onboard UAVs are increasingly being used for vegetation mapping (Laliberte et al., 2011; Pádua et al., 2017; Bonnet et al., 2017).

Recently, the UAV-RS approach has been frequently reported as advantageous over spaceborne and traditional airborne remote sensing approaches due to the resultant high temporal and spatial resolution data as well as the survey cost efficiency associated with this approach (Femondino et al., 2011; Müllerová et al., 2017; Babapour et al., 2017). Applications of the UAV-RS approach include *inter alia* agriculture (Li et al., 2017), precision agriculture (Primicerio et al., 2012; Gómez-Candón et al., 2014; Rokhmana, 2015; Bagheri, 2016; Puri et al., 2017), land use (Akar, 2017), forestry (Thiel et al., 2017; Torresan, et al., 2017), archaeology (Rinaudo et al., 2012; Fernández-Hernandez et al., 2015), classification of native vegetation and mapping of invasive alien plants (IAPs) (Dvořák et al., 2015; Müllerová et al., 2016; Hill et al., 2017).

Like airborne and satellite imagery, UAV imagery needs to be geometric and radiometric calibrated so as to ensure its spatial accuracy as well as scientific integrity. Geometric corrections, in particular, are necessary because (1) UAV systems are light in weight and this results in unstable flights depending on the wind speed and direction, (2) due to their payloads, use of non-metric cameras with no geometric calibration certificates is often made (Kelcey and Lucieer, 2012; Yang et al., 2017). On the other hand, radiometric corrections are also necessary because, to have lasting quantitative value, it is standard practice to have remotely sensed data calibrated to physical units of reflectance (Smith and Milton, 1999). The radiometric calibration process converts image digital numbers (DNs) to at-surface reflectance units so as to enable quantitative analysis across data acquired at

different seasons or times of the day as well as by different sensors. Calibrated datasets may be cross compared because while image DNs of a target object change depending on environmental factors. These factors include but are not limited the incoming irradiance and atmospheric conditions (Honkavaara et al. 2017). After radiometric calibration, the spectral characterization of an object becomes possible (Kelcey and Lucieer, 2012; Crusiol et al., 2017). Moreover, radiometric calibration improves the accuracy of derived vegetation indices as well as derived biochemical and biophysical parameters (Nguyen et al., 2015).

Nevertheless, most studies that applied the UAV-RS for IAPs monitoring made use of thematic image classification without either conducting geometric or radiometric calibration (Dvořák et al., 2015; Müllerová et al., 2016 and Mafanya et al., 2017). This is because UAV-RS of biological invasions should be optimized to be time and cost efficient so as to enable mapping of IAPs at the right phenological stage, at an affordable cost and with a quick turnover (Müllerová et al., 2017; Hill et al., 2017). However, monitoring of IAPs could encompass not only qualitative thematic mapping but also quantitative image analysis such as image band mathematics (e.g. vegetation indices) as applied *inter alia* in agriculture (Li et al., 2017), precision agriculture (Honkavaara et al., 2013, Candiago et al., 2015; Sonaa et al., 2016) and forestry (Thiel et al., 2017; Torresan, et al., 2017). Since one of the aims in UAV-RS is cost reduction, a radiometric calibration method for UAV based IAPs monitoring ought to be cost and time efficient. A large scale radiometric calibration method that is timely and less costly is proposed in this framework.

The production of thematic maps for classifying IAPs in UAV-RS is either pixel based or follows OBIA and sometimes utility of a hybrid approach is made (Mafanya et al., 2017; Dvořák et al., 2015). In particular, pixel based image classification makes use of either parametric or non-parametric classifiers to assign pixels to a particular class. While the pixel based image classifiers assign pixels to classes, object based image classifiers assign objects or segments to a particular class, instead of pixels. Both pixel and object based image classifiers can be either supervised or unsupervised. This research work evaluated both pixel and object based image classification techniques for mapping *H. pomanensis*.

1.2. Problem statement

H. pomanensis was detected by the South African National Biodiversity Institute: Invasive Species Programme (SANBI ISP) in 2011 as part of on-going efforts at incursion response planning (Wilson et al., 2013). This plant colonises farms making it hard for farmers to use the land for cropping, block the mobility of livestock, injure animals and reduce grazing land. This plant invasion has been spotted by SANBI ISP field teams in a farming area of not less than 10 000ha. *H. pomanensis* is a category 1a IAP meaning that, by law, it is compulsory to eradicate the plant from the land in South Africa (SANBI, 2018).

The traditional GPS based field campaigns for mapping IAPs are costly, time consuming and labour intensive (Kaneko and Nohara, 2014). To reduce work load, sampling methods are usually adopted and the results may not depict the actual status quo of IAPs invasion. Since the mid-1990s, remote sensing techniques have been used to detect and quantify the spatial extent of IAPS (Haung and Asner, 2009). The challenge is that IAPs monitoring needs high spatial/spectral resolution data at specific phenological stages during which satellite or airborne data may not be available or be available at a coarser resolution (Müllerová et al., 2013). The miniaturization of GNSS/INS systems and barometers means that spatial data can be acquired using UAVs (Wan et al., 2014). Dvořák et al. (2015) suggest that UAVs can be used for thematic mapping of IAPS as they provide high spatial resolution data timely and flexibly. Thus this study proposes a semi-automated object based image classification UAV-RS framework for mapping IAPs in South Africa using H. *pomanensis* as a case study.

1.3. Study aim and objectives

The aim of this study is to propose a UAV-RS framework for semi-automated object-based image classification of invasive alien plant species in South Africa using *H. pomanensis* as a case study. The objectives of the study involve;

- Proposing a large scale UAV-RS radiometric calibration method that is time and cost efficient,
- evaluating pixel- and object-based image classifiers to determine the best performing image classifier for mapping *H. pomanensis*,
- determining whether radiometric calibration improves image classification accuracy.

1.4. Study area and species description

1.4.1. Study area

The study area is located near the Alldays town within the Waterberg district municipality of the Limpopo province of South Africa (Figure 1a). The area is characterised by (i) a semi-arid climate, (ii) summer rainfall, and (iii) average midday temperatures of 22.3 °C and 31.9 °C in winter (June to August) and summer (October to February) seasons, respectively (Mzezwa, 2010). The rainfall ranges from a few mm in winter and could escalate to a maximum of approximately 81mm in summer (Mzezwa, 2010). A subset of the 97ha mapped area is shown in Figure 1b. The study area is a flat terrain with orthometric height values ranging from 800m to 817m. Tree species that occur in this heterogeneous semi-arid woodland include *Commiphora mollis* (Velvet-leaved corkwood), *Commiphora neglecta* (Green-temmed corkwood), *Commiphora schimperi* (Glossy-leaved corkwood), *Commiphora viminea* (Zebra-bared corkwood), *Acacia nolitica* (Scented pod thorn), *Acacia tortilis* (Umbrella thorn), *Acacia nigrescens* (Knob thorn), *Acacia robusta* (Broad pod robust thorn), *Acacia mellifera* (Black thorn), *Balanites maughamii* (Green thorn), *Albizia sp.* (False thorn), *Kirkia acuminata* (White seringa), *Combretum imberde* (Leadwood), *Combretum hereroense* (Russet bush willow), *Boscia albitrunca* (Shepherd's tree), *Berchemia zeyheri* (Red ivory), *Maerua angolensis* (Bead bean), *Lannea sp*. (False Marula), *Sclerocarya birrea* (Marula) and *Opuntia humifusa* (Devil's tongue), amongst others (Mafanya et al., 2017). The *Harrisia pomanensis* invasive plant forms dense clusters in the described woodland area and could consequently replace pasture, injure animals and thus inhibit cropping and grazing (Wilson et al., 2013). *Harrisia pomanensis* (*H. pomanensis*), commonly known as the Midnight Lady is a succulent cactus with jointed spiny fleshy stems and thorny spikes.

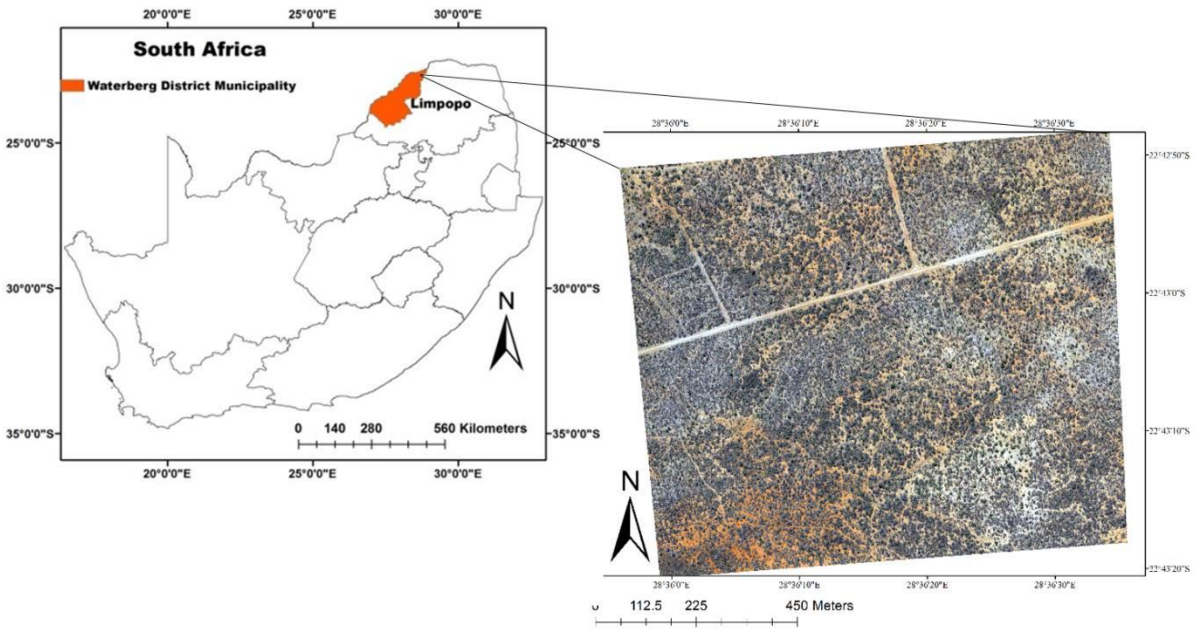

Figure 2: a) Map of South Africa showing the location of Waterberg district municipality within the Limpopo province and b) a subset of the UAV-derived ultra-high spatial resolution (5cm) RGB orthomosaic.

1.4.2. Species description

The genus *Harrisia* (Cactaceae) compromises 20 known species native to South America, the Caribbean, Florida and the West Indies (Franck et al., 2013). *Harrisia* cacti are succulent plants with spikes and produce fruits with hundreds of black seeds. The fruit can be dispersed by birds and animals and this is one of the ways by which cacti spread. The genus species have jointed spiny fleshy stems with thorny spikes and when these stems touch the ground, they develop roots and this is another way cacti spread (DAF, 2013). Most Cacti were introduced in South Africa exclusively for ornamental purposes (Novoa et al., 2015). *Harrisia pomanensis* (*H. pomanensis*), commonly known as the Midnight lady is a succulent cactus that belongs to the *Harrisia* genus (Figure 2a,b,c,). *H. pomanensis* plants have jointed spiny fleshy stems with thorny spikes and when these stems touch the ground, they develop roots and spread.


a)

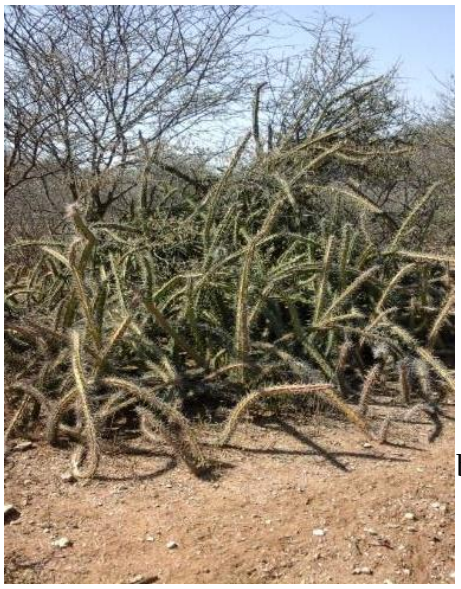
b)


c)

Figure 3: *H. pomanensis* photos a) and b) showing clusters and c) showing stems.

CHAPTER 2

2. Literature Review

2.1. Introduction

This chapter reviews previous remote sensing applications for mapping and monitoring invasive alien plants (IAPs). Firstly, consideration was made for application of spaceborne hyperspectral and multispectral sensors in studying IAPs. Secondly, airborne hyperspectral and multispectral sensors are discussed in relation to IAPs monitoring. Thirdly, a review of the use of Unmanned Aerial Vehicles (UAVs) as a platform for IAPs monitoring is provided. For each section, relevant sensors are compared in a tabular format so as to show the relevant system design and associated sensor resolutions. Finally, the mapping workflows based consumer grade digital camera mapping were evaluated with special focus on image processing, calibration, classification as well as accuracy assessment methods.

2.2. Background

Historically, IAPs monitoring was inefficient, expensive and time consuming (Jay et al., 2009). The use of RS in the study of IAPs was encountered in the mid 1990's relative to large-scale ecological studies (Huang and Asner, 2009). This was due to the realisation that RS can be used to effectively map and monitor IAPs not only at large regional scale but also suitable for local scale, particularly at species specific level. There are two main optical RS approaches for mapping and monitoring IAPs, namely, high spectral resolution with low spatial resolution and high spatial resolution with low spectral resolution (Underwood et al., 2003). In particular, the high spectral resolution approach entails the use of hyperspectral sensors for collecting hundreds of narrow bands (less than 10 nm bandwidth) in the visible, near infrared and shortwave infrared regions of the electromagnetic spectrum (Agjee et al., 2015). On the other hand, the high spatial resolution approach usually makes use of spaceborne and/or airborne multispectral imagery whose spatial resolution can be as high as 2 m, for instance in the case of WorldView-2 (Ngubane et al., 2014).

2.3. Spaceborne hyperspectral IAPs monitoring

Customarily, the spaceborne hyperspectral RS technique is used in conjunction with *in situ* measured spectral data. The use of proximally sensed spectral data helps to spectrally calibrate remotely sensed hyperspectral data and act as a reference validation data for spectral accuracy assessment (Rao, 2008). The *in situ* spectral data can also be used to determine the optimal narrow bands for discriminating certain plant species from their co-habitant plants and the best phenological time for discrimination (Tesfamichael et al., 2017). For example, Ustin and Santos (2010) used field and spaceborne spectroscopy to distinguish between native and non-native plant species based on their relative spectral signatures. Further, the study showed that Analytical Spectral Devices (ASD, Inc., Boulder, CO) FieldSpec-3 *in situ* spectral measurements complement Airborne Visible/Infrared Spectrometer (AVIRIS) and HyMap hyperspectral data by providing information about individual species at ground level. The main advantage for using hyperspectral data is that detailed spectral signatures can be profiled and use of specific regions can be made to distinguish between native plants and IAPs (Ustin and Santos, 2010).

In addition to combining proximally and remotely sensed passive optical data , hyperspectral data can be fused with 3 dimensional digital surface models (3D DSMs) from active remotely sensed data. For instance, Huang and Asner (2009) fused light detection and ranging (LiDAR) data and hyperspectral imagery to delineate the structural and functional properties of IAPs in Hawaii, United States of America (USA). The study reported in Huang and Asner (2009) demonstrated that hyperspectral data can be used to accurately delineate IAPs. Furthermore, Williams and Hunt (2004) reported a 95% overall accuracy for mapping Leafy Spurge (Euphorbia esula) using a specialized spectral mixture analysis (SMA) on AVIRIS hyperspectral data.

Although the history of hyperspectral RS is relatively short (< 40 years) compared to aerial photography (> 100 years) and spaceborne multispectral RS (~ 50 years), hyperspectral data are one of the most heavily used imaging sources for mapping and monitoring IAPs (Huang and Asner, 2009). This is observed in the studies by DiPietro, (2002); DiPietro et al., (2002); Underwood et al., (2003, 2006a, 2006b); Andrew and Ustin, (2006, 2008, 2009a, b); Hestir et al., 2008; Noujdina and Ustin, (2008) and Nguyen et al., (2011). Notwithstanding these efforts, the problem with using proximally sensed spectral data in conjuction with spaceborne hyperspectral data is that for the same object, the scale of the *in situ* field spectra

usually does not match the scale of the spaceborne imaging spectroradiometer.This can be attributed to the relatively coarser spatial resolution associated with spaceborne hyperspectral sensors (~30m) (Table 1). Moreover, there are sometimes geometric distortions or misalignments between hyperspectral imagery and 3D LiDAR data (Huang and Asner, 2009).

The resolution trade-offs in optical RS are evident in spaceborne hyperspectral sensors (Lefsky and Cohen, 2003). For instance all the reviewed sensors in Table 1 have very high radiometric and spectral resolutions but low spatial resolutions (mostly 30m). On the other hand, the sensor with the highest spatial resolution (HyMap due to its lower orbital altitude) has the lowest spectral resolution among the sensors listed Table 1. The additional EnMap and DESIS sensors are the planned commercial hyperspectral imagers which will be commissioned by the German Aerospace Center Deutsches Zentrum für Luft- und Raumfahrt e.V. (DLR) in 2018 and 2020, respectively (Gaunter et al., 2015; Muller et al., 2016).

Table 1: Selected spaceborne hyperspectral sensors and their respective resolutions

Sensor	Altitude	Spatial Res.	Spectral Res.	Spectral bands	Spectral Range	Reference
Hyperion	705km	30m	10nm	220	350-2500nm	NASA (2017)
AVIRIS	20km	20m	9.5-10nm	224	400-2500nm	NASA (2017)
HyMap	1-5km	2-10m	15-17nm	128	450-2500nm	Cocks et al., (1998)
EnMap	652km	30m	6-14nm	250	420-2450nm	Gaunter et al., (2015)
DESIS	400km	30m	2.55nm	240	400-1000nm	Muller et al., (2016)

2.4. Airborne hyperspectral IAPs monitoring

The airborne hyperspectral remotely sensed data is mostly acquired at higher spatial resolutions (as high as 10 cm depending on flying height and sensor characteristics) and therefore the inherent scale problem associated with combining spaceborne remotely sensed and *in situ* proximally sensed spectral data is less profound (Miguel et al., 2014). As a result, airborne hyperspectral remotely sensed data tend to be more spectrally accurate compared to their spaceborne counter parts when mapping at smaller scales. For instance, Laurin et al., (2014) used the AISA Eagle sensor with 244 bands in the range 400-1000nm with spectral and spatial resolution of 2.3 nm and 1 m, respectively. At such high imaging spatial

resolution, the *in situ* spectral data scale can be easily resampled to match the airborne hyperspectral image data.

Unlike spaceborne sensors, airborne hyperspectral sensors are usually mounted on manned aircraft together with LiDAR scanners. The fusion of airborne hyperspectral and LiDAR data allows for even greater opportunities due to mapping scale compatibility. For instance, the LiDAR point cloud data can be rasterized to 3D DSM with a comparable spatial resolution with the hyperspectral data.

For example, Chance et al. (2016) combined (1) LiDAR DSM derived attributes, (2) 1m spatial resolution Compact Airborne Spectrographic Imagery (CASI 1500) and (3) full range ASD proximally sensed spectral data and achieved an overall accuracy of 87.1% for the random forest (RF) detection models. The study demonstrated that LiDAR data and hyperspectral data are applicable for large scale mapping and monitoring of IAPs for the Himalayan blackberry (*Rubus armeniacus*) and English ivy (*Hedera helix*) invasive plants. Notwithstanding previous successful attempts to use hyperspectral data for mapping IAPs, several limitations ought to be taken into cognisance. The limitations include the high cost of airborne hyperspectral sensors and portable spectrometers, as well as the resultant large volumes of data that require high computing power for processing (Agjee et al., 2015).

Efforts to reduce the cost of hyperspectral sensors and operational costs are currently underway (e.g. mounting hyperspectral sensors on UAVs or piloted light aircrafts). For example, Calvino-Cancela et al. (2014) developed a customized hyperspectral imager with 200 bands in the range 380-1000nm with a bandwidth or spectral resolution of 3nm and a spatial resolution of 5cm. The sensor is light in weight and can be mounted on an ultralight aircraft (e.g. a gyrocopter). The study achieved user and producer accuracies that are greater than 90% for mapping *Acacia melanoxylon, Oxalis pes-caprae, Carpobrotus aff. edulis* and *Acinaciformis*. Recently, there has been an increasing number of affordable commercial compact imaging spectroradiometers for mounting on aircrafts, light aircrafts and UAVs. Table 2 lists some selected affordable compact imaging spectroradiometers with their respective Signal to Noise Ratios (SNRs) for utility in airborne hyperspectral remote sensing.

Table 2: Airborne spectroradiometers with their respective frame rates, Signal to Noise Ratios and spectral resolution

Sensor	Frame Rate	SNR	Spectral Res.	Spectral bands	Spectral Range	Producer
Hyperspec E	160Hz		1.5nm	923	380-1000nm	Headwall
Pika XC2	165Hz	366:1 to 518:1	1.3nm	447	400-1000nm	Resonon
HySpex VNIR 1800	260Hz	255.01:1	3.26nm	182	400-1000nm	Hyspex
Pika NIR	520Hz	1885.0:1	4.9nm	164	900-1700nm	Resonon
Hyperspec SWIR	450Hz		10nm	267	950-2500nm	Headwall
Hyspex SWIR	400Hz	1100.0:1	5.45nm	288	930-2500nm	Hyspex

2.5. Spaceborne multispectral IAPs monitoring

Recent technological improvements in spaceborne multispectral sensors have afforded the remote sensing community with the opportunity to explore more image wavebands at higher spatial resolutions. As a result, the efficacy of using these datasets for IAPs monitoring has been tested in various studies across the world. For example, the strategically placed 8 bands of the 2m spatial resolution Worldview-2 data were tested for efficacy in mapping the arid rangeland invasive plant, Buffel grass (*Centhrus ciliaris*) in Australia (Marshall et al., 2012). The study assessed whether the additional bands in Worldview-2 increased the spectral separability and discrimination between native arid rangeland grass species and the invasive Buffel grass. The analysis was done between a 4 band stack (i.e. with blue, green, red and NIR1 wavebands) and a full 8 waveband stack. The study found that the additional bands increase the vegetation discrimination, only marginally but provided less commission errors. Moreover, Dlamini (2010) tested the efficacy of the Worldview-2's newer bands for mapping two problem IAPs, *C. odorata* and *L. camara* in Swaziland. The study made use of probabilistic Bayesian networks to detect the invasive plants and found higher classification accuracies when using the newer bands. The Worldview-2 additional bands were also applied in South Africa for mapping Bracken fern (*Pteridium aquilinum L.Kuhn*), an IAP that

suppresses native plants in the KwaZulu Natal Sandstone Sourveld (Ngubane et al., 2013). The study obtained 79.14%, 97.62% and 91.11% for the overall, user and producer accuracies, respectively, using the random forest algorithm. Table 3 lists some selected spaceborne multispectral sensors with their respective orbital altitudes and resolution characteristics.

The efficacy of spaceborne multispectral imagery is mostly observed when mapping canopy dominating IAPs or species that are phenologically different from the background vegetation. However, spaceborne multispectral data have been reported to perform relatively poor for mapping understorey IAPs (Fox et al., 2009). Moreover, the relatively low spectral resolution limits the application of multispectral satellite imagery in the monitoring of species specific IAPs especially when the species of concern is phenologically invariant from its background vegetation (Peerbhay et al., 2016). Reportedly, hyperspectral data performs better than multispectral data for differentiating IAPs from native background vegetation. For instance, QuickBird image data was surpassed by AISA hyperspectral data in mapping Saltcedar in the Rio Grande floodplain, USA (Wang et al., 2013).The difficulty in mapping understory IAPs has been frequently identified in RS research (Fox et al., 2009; Peerbhay et al., 2016; Huang and Asner, 2009). Remote Sensing methods for improving detection of understorey IAPs have been presented by Joshi et al. (2006), Wang et al. (2009) and Tuanmu et al. (2010).

Table 3: Selected spaceborne multispectral sensors with their respective orbital altitudes and resolution characteristics.

Sensor	Altitude (km)	Spatial Resolution	Pan Band Spatial Resolution	Spectral Resolution	Spectral bands
Landsat-8	705	30m	15m	20nm - 60nm	8
Sentinel-2	786	10,20&60m		15nm-180nm	13
SPOT-6/7	660	6m	1.5m	60nm-180nm	4
QuickBird	450	2.4m	0.65m	60nm-140nm	4
Worldview-3/4	617	1.24m	0.31	40nm-180nm	8

2.6. Airborne multispectral IAPs monitoring

The use of large- and medium-format photogrammetric cameras in airborne multispectral imaging provides more pixels (image sizes at least 1280 x 1024) and thus allowing high spatial resolution remote sensing from the airborne platform (Wiechert et al., 2011). Chance et al., (2016) showed that LiDAR data coupled with airborne multispectral data has the potential to improve vegetation classification accuracy. This is because LiDAR derived 3D DSMs can be used to discriminate vegetation based on height metrics. For instance, Hantson et al., (2012) used LiDAR data and the large-format UltraCam-X at 0.25m spatial resolution to classify invasive woody species in coastal dunes in the Netherlands. The LiDAR data was used to create a Canopy Height Model (CHM) for dune shrub classification. The incorporation of the LiDAR datasets increased classification accuracy by 10% when compared to classification based solely on optical imagery. Another study by Hellesen et al., (2013) applied decision trees and OBIA on UltraCam-Xp colour infrared (CIR) imagery. In the study, LiDAR data was utilized to crop out the invasive shrubs and then image classification was performed on the 0.16m spatial resolution CIR imagery. The cropping of shrubs based on height metrics was conducted because shrubs are sometimes spectrally similar to native vegetation and thus removing background vegetation before applying image classification techniques improved classification accuracy.

The fusion of airborne multispectral with LiDAR data increases the efficacy of this particular avenue of remote sensing applications. However, the costs associated with large-format metric cameras and LiDAR sensors may deem these tools unattractive to IAPs managers and researchers. Nevertheless, medium-format cameras such as Tetracam cameras are much more affordable. The large format and medium format metric cameras have a lot of potential for IAPs monitoring due to the increased spatial resolution which results from the many pixels these sensors offer. Table 4 lists selected airborne multispectral cameras that can be available to IAPs managers. The large format cameras have a better spectral and spatial resolution than the medium format cameras as can be seen in Table 4. However, the medium format camera can also be mounted on UAV because they are light in weight and may have sufficient spatial and spectral resolutions for specific small scale mapping applications and are generally much more affordable.

Table 4: Selected airborne large- and medium-format cameras with their respective resolutions.

Format	Sensor	Image size (n x n pixels)	Spectral Res.	Spectral bands	Producer
Large	ADS 100	20,000 x 20,000	30nm	R,G,B,NIR	Leica
	UltraCam-Xp	17,310 x 11,310	6nm	R,G,B,NIR	Vexcel Imaging
	DMC II 250	17,216 x 14,656	7.2nm	R,G,B,IR	Intergraph
Medium	RCD 30 (80Mpixels)	10320 x 7752		R,G,B,NIR	Leica
	DSS 580(dual cam)	7752 x10320		R,G,B +NIR	Trimble
	Double DigiCam 100	11,608*8,708		R,G,B +CIR	Integrated Geospatial Innovations

2.7. UAV-borne hyperspectral IAPs monitoring

Recently, the UAV-RS approach has been frequently reported as advantageous over spaceborne and traditional airborne RS approaches due to the associated high temporal and spatial resolutions as well as the survey cost efficiency (Femondino et al., 2011; Müllerová et al., 2017; Babapour et al., 2017). Rapid technological advances in the miniaturization of sensors means that light weight hyperspectral sensors can be mounted onto monitoring UAV systems (Mitchell et al., 2012). Just like spaceborne and airborne imaging spectroradiometers, UAV-borne hyperspectral sensors are sometimes used in conjuction with proximally sensed *in situ* spectral data. For example, Bareth et al., (2015) used the ASD FieldSpec3 *in situ* data to validate UAV derived spectral data measured from two different airborne spectroradiometers. The study demonstrated that with the miniaturization of airborne

sensors, extraction of single plant attributes is possible and the spectral signatures derived from compact light weight hyperspectral sensors are comparable within 1 standard deviation of the proximally sensed *in situ* spectral data. As done in traditional airborne hyperspectral remote sensing, UAV-borne hyperspectral data can be fused with LiDAR data for individual plant species identification and 3D characterization at sub-meter scales (Sankey et al., 2017).

The monitoring of IAPs should be customized to be time and cost efficient so as to enable managers to map IAPs at the right phenological stage, at an affordable cost and with a quick turnover (Dvořák et al., 2015). To fulfil these requirements, Jay et al., (2009) developed an affordable low cost hyperspectral sensor (Resonon Pika II) with a spectral range of 400-900nm (i.e. VNIR) and a spectral resolution of 2.1nm per narrow waveband for UAV systems. The sensor reportedly mapped Leafy spurge (*Euphorbia esula*) patches in a rangeland at relatively high accuracies reaching 79% when flowering of the Leafy spurge was at its high peak in July. This demonstrates that the phenological stage is an important consideration when mapping IAPs. The results achieved in the study were comparable to results of traditional airborne spectroscopy even though the authors utilized a low cost UAV-borne sensor (Jay et al., 2009).

Another cost effective hyperspectral sensor for rapid identification and monitoring of IAPs was tested by mapping the spatial distribution of Paterson's curse (*Echium plantagineum*),Wild oats (*Avena spp*.), Barley grass (*Hordeum spp*.), Phalaris (*Phalaris aquatica*), Annual ryegrass *(Lolium rigidum*), Great brome (*Bromus hordeaceus*), Spear thistle (Cirsium vulgare), and St Barnaby's thistle (*Centaurea solstitialis*) in Australia (Dehaan et al., 2012). The sensor was the Headwall hyperspectral Visible Near-Infrared (VNIR) imaging optical spectroradiometer. The authors used the Mixture Tuned Matched Filtering (MTMF) algorithm to map IAPs from background vegetation and achieved overall accuracies ranging from 65% to 85%. The lower overall accuracies were attributed to spectral mixing because the mapping algorithm correctly classified IAPs in unmixed pixels of the hyperspectral imagery (Dehaan et al., 2012).

Notwithstanding these successes, one problem associated with using UAV derived hyperspectral imagery in conjunction with *in situ* measured spectra is the poor spectral calibration due to spectral shifts between the remotely sensed imagery and *in situ* proximally sensed spectral signatures (Bareth et al., 2015). To address this problem, Liu et al. (2014) adopted spectral calibration methods that are usually applied on spaceborne hyperspectral data on UAV derived hyperspectral data and managed to determine and correct shifts both at the spectral centre wavelength position and at the full-width at half-maximum (FWHM)

position. Vicarious spectral calibration methods whereby calibration targets are placed on the ground can be used to force the UAV derived hyperspectral data to match *in situ* proximally sensed spectra for the same targets (Dehaan, 2012). There are sometimes pixel geometric misalignments between accuracy assessment data and hyperspectral data, especially when the reference data used is high resolution aerial photographs (Dehaan et al., 2012). Despite these challenges, UAV-borne hyperspectral monitoring of IAPs might be perceived as a better applicable practical solution due to the associated low survey costs and quick turnover. Table 5 lists selected small light weight hyperspectral sensors that IAPs managers can consider for incorporating in UAV systems.

Table 5: Selected lightweight UAV hyperspectral sensors with their respective resolutions.

Sensor	Weight (Kg)	Frame rate (Hz)	Number of Spatial bands	Number of Spectral bands	Spectral res. (nm)	Company
Nano-Hyperspec	0.52	350	640	270	2.2	Headwall
Pika L	0.6	249	900	281	2.1	Resonon
SOC710-GX	1.8	90	640	120	4.2	Surface Optics
Pika XC2	2.7	165	320	164	1.3	Resonon
VNIR-1024	4.2	690	1024	108	5.4	HySpex

2.8. UAV-borne multispectral IAPS monitoring

UAV-borne light weight multispectral sensors offer the opportunity to provide accurate mapping of the spatial distribution of IAPs. Currently, UAV-borne multispectral sensors need to weigh less than 5 kg because multirotor and fixed wing UAVs have payloads in the range 1 to 2kg) and 1-5kg, respectively, with the exception of mini-UAVs whose payloads are between 0.2 and 1.5 kg (Bendig et al., 2012). Bendig et al., (2012) introduced the concept of mini-UAVs using the MK-Okto small aircraft equipped with a Tetracam Mini MCA camera whose weight is less than 700g. The Tetracam Mini MCA UAV-borne multispectral sensor was also used by Slaughter (2014) to map and monitor the spatial distribution of Lehmann lovegrass (*Eragrostis lehmanniana*) in Walnut Gulch and Jornada, USA. The study used

OBIA image classification with two segmentation stages (i.e. multiresolution first followed by spectral difference segmentation) and two classification methods (i.e. Rule based or Nearest Neighbour classification) in eCognition (Slaughter, 2014). The accuracy assessment resulted in overall accuracies of 93% and 88% for mapping Lehmann lovegrass in Walnut Gulch and Jornada, respectively (Slaughter, 2014). The study demonstrated that Lehmann lovegrass can be identified, detected and mapped using a multispectral sensor on board a UAV. Following these attempts, another light weight UAV-borne multispectral camera, a 5 band MicaSense Red Edge (MSRE) was used to map the invasive Common reed (*Phragmites*) in the Gulf of Mexico (Samiappan et al., 2017). The analysis methodology utilized a pixel based support vector machine (SVM) classification on the blue, green, red, red edge, and near-infrared bands of the MSRE and achieved a 91% overall accuracy. Table 6 lists some selected lightweight UAV multispectral sensors with their respective weights, resolutions characteristics and number of spectral bands. A recurring challenge in UAV-borne multispectral imaging is that of payload because the multispectral sensors need to be light in weight to enable mounting on UAV systems (Bendig et al., 2012).

Table 6: Selected lightweight UAV multispectral sensors with their respective weights, resolutions characteristics and number of spectral bands.

Sensor	Weight (kg)	GSD at 120m AGL (cm)	Spectral bands	Image depth (bit)	Company
RedEdge	0.18	8	R,G,B,Red Edge, NIR	12	MicaSense
uMCA-6	0.53	6.6	R,G,B,2xRed Edge, NIR	10	Tetracam
MultiSPEC 4C	0.9	10	R,G,Red Edge,NIR	10	SenseFly
Sequoia	0.135	11	R,G,Red Edge, NIR	10	Parrot

2.9. UAV-borne consumer grade digital cameras for IAPs monitoring

Most successful studies in mapping IAPs used very high spatial resolution imagery i.e. ≤ 5cm (Metternicht, 2007). Such high spatial resolution imagery, particularly captured using

consumer grade digital cameras (CGDCs) on-board UAVs have several advantages for accurately mapping IAPs when compared to manned aircraft or spaceborne platforms. These advantages include flexible temporal resolution and low data acquisition costs (Dvořák et al., 2015). The CGDCs are becoming a mapping tool of choice for IAPs monitoring managers due to the associated low survey costs as well as high spatial and temporal resolutions (Tamouridou et al., 2017).

Furthermore, CGDCs are often converted or modified to sense the near infrared (NIR) portion of the electromagnetic spectrum as modern CMOS and CCD sensors are sensitive to this type of radiation. For example, in the Czech Republic, Dvořák et al. (2015) developed a rapid, repeatable and efficient UAV based system for mapping and monitoring of IAPs from an unmodified and a modified CGDC. The Canon Power Shot S100 CDGC was modified to acquire NIR imagery by removing the standard "heat mirror" infrared (IR) cutting filter and replacing it with a 720nm IR filter such that the first band is NIR instead of the red waveband (Dvořák et al. 2015).The efficacy and applicability of the system was tested by mapping selected species covering the range of variability of life forms from herbs to trees, forming distinct shape features (*giant hogweed*), stands with complicated leaf architecture (*knotweeds*), small or larger trees (tree of heaven and black locust), or plants with particular inflorescence *(giant hogweed and black locust*). The research work showed that the developed UAV based system produces results that are comparable to traditional and manned aircraft or spaceborne platforms.

Notwithstanding the progress in UAV-based RS, several challenges such as geometric and radiometric issues, high amount of data to be processed and legal constrains for the UAV flight missions over urban areas ought to be considered carefully. The geometric distortions in UAV imagery are due to the fact that UAV systems are light weighted and therefore, susceptible to tilts due to prevailing winds and this affects the platform altitude and attitude. In particular, unstable flights affect camera exterior orientation parameters and results in off nadir photos. One way to overcome tilts and vibrations is to mount the camera on a three axis gimbal that is integrated with the UAV's inertial navigation system (INS) so as to stabilize the camera during the UAV flight (Hill et al., 2017).

Müllerová et al., (2017) compared detection accuracies between Worldview-2 data and an orthomosaics derived from unmodified and modified CGDC for mapping Black locust (*Robinia pseudo accacia*).

CHAPTER 3

3. Methodological Framework

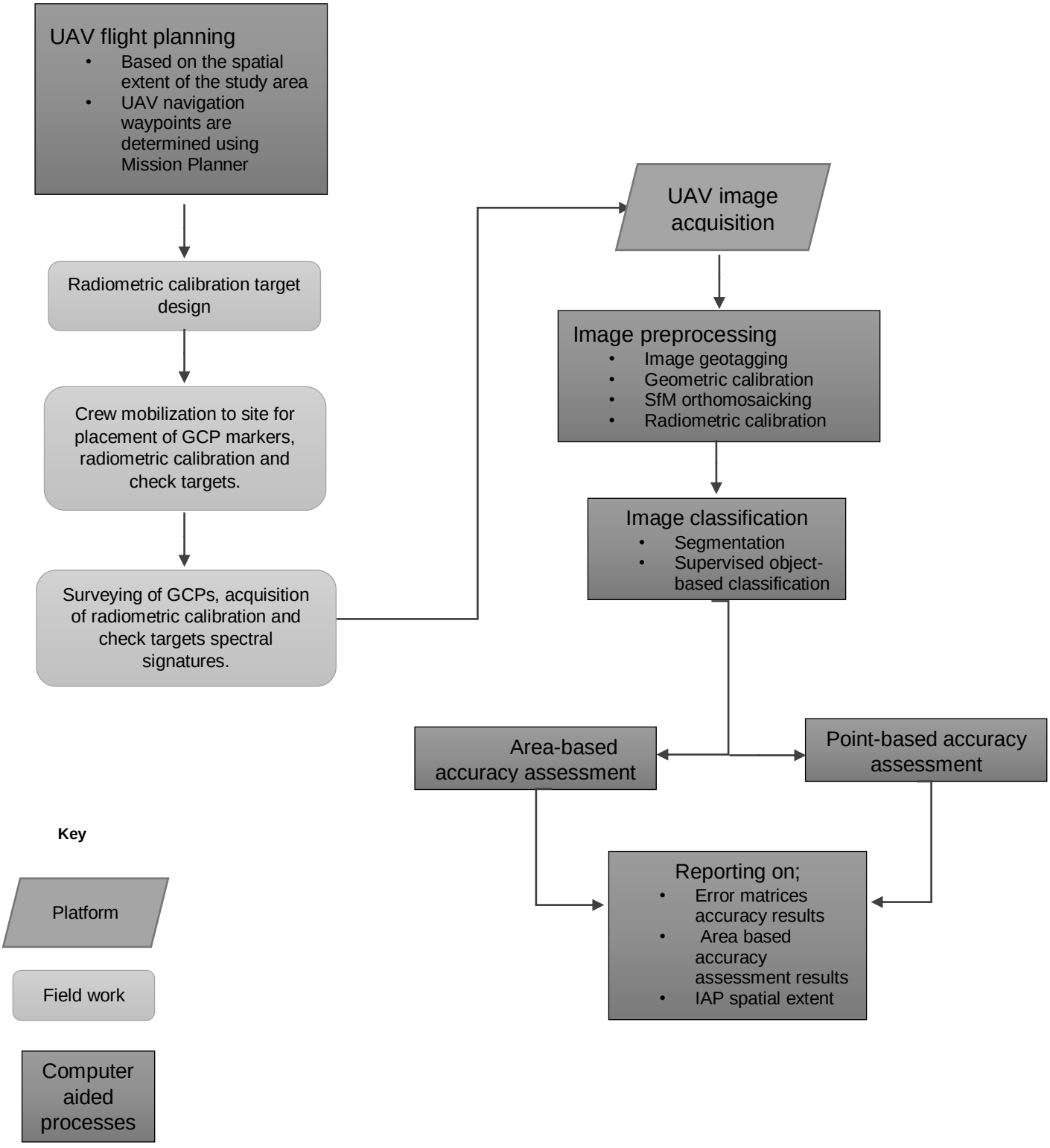

Figure 4: The proposed framework for semi-automated object-based image classification of invasive alien plant species in South Africa using *H. pomanensis* as a case study.

This framework uses the UAV-RS approach for mapping IAPs since traditional field

based methods have been deemed to be time and labour intensive. The proposed framework involves image acquisition, pre-processing and analyses using OBIA since this approach has been found to be effective for classifying high resolution images. The methodology chapter (Chapter 4) describes all the GCP logging and image acquisition, pre-processing and classification procedures involved in this framework. The point- and area-based accuracy assessment approaches adapted in this framework are also described in chapter 4.5.

3.2. Geometric calibration

The UAV-RS approach that makes use of non-metric digital cameras requires automatic self-calibration software applications (such as Photomodeler, Agisoft Lens, iWitness, MicMac, and 3DF Zephir) to estimate the intrinsic camera parameters as this information is normally unavailable to the camera user (Balleti et al., 2014). In this study, the Agisoft Lens software package to determine of the camera interior orientation parameters. Agisoft Lens software estimates four calibration parameters for correcting tangential distortion, namely (i) horizontal focal length (in pixels), (ii) vertical focal length (in pixels), (iii) X co-ordinate of the principal point and (iv) the Y co-ordinate of the principal point. The distortion model used for correcting radial distortions in the Agisoft Lens software is the Brown's model which compensates for the imperfect lens centre (Agisoft LCC, 2018). During this process, a black and white chessboard calibration target is displayed on the LCD screen (Figure 3). Five photos (the minimum is three) are then captured from different angles to estimate both tangential and radial distortions as per Figure 4. The camera intrinsic parameters are then saved in XML format to be imported in the camera calibration window in Agisoft Photoscan for use in Structure from Motion (SfM) image mosaicking.

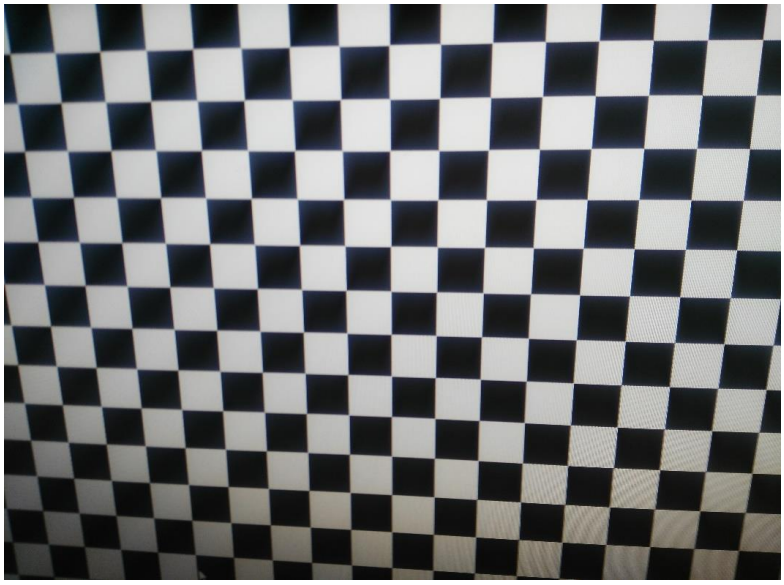

Figure 5: Geometric calibration target image displayed on a computer LCD screen.

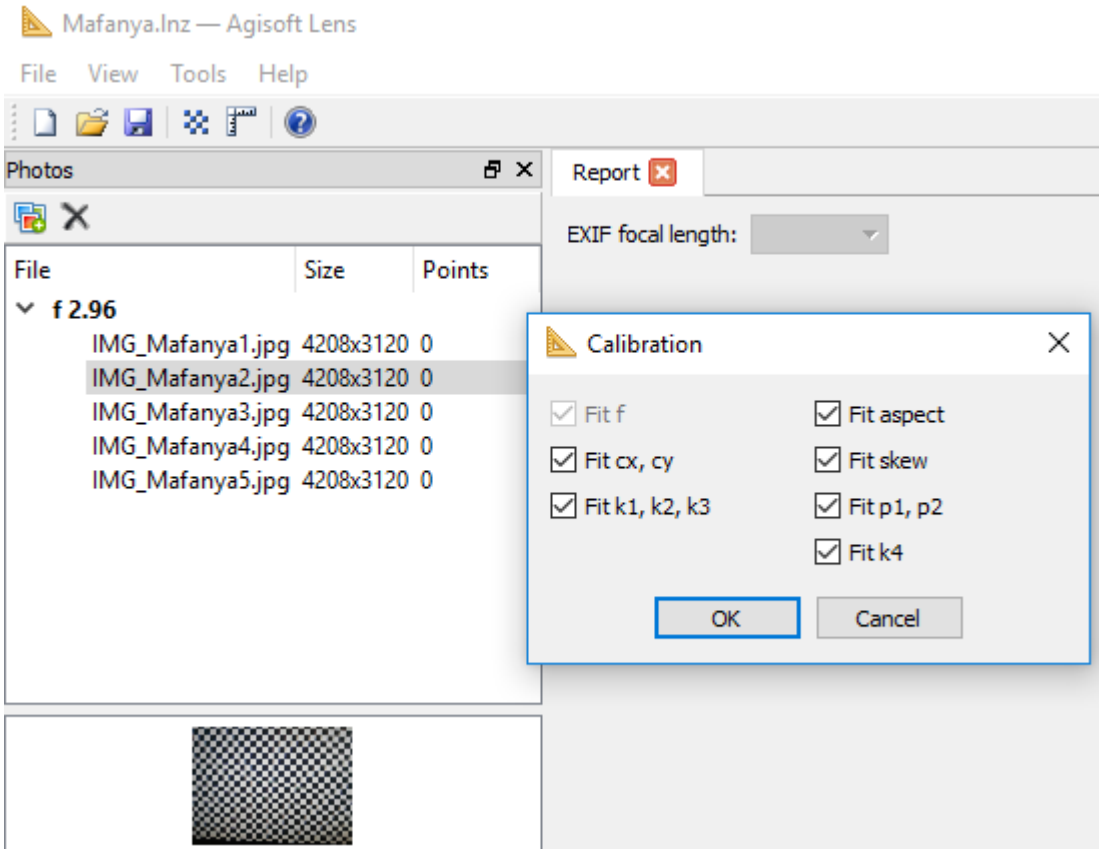

Figure 6: Demonstration of the Agisoft Lens calibration process using 5 photos.

3.3. Structure from Motion image mosaicking

3.3.1. Acquisition of Ground Control Points

In this study, ground control points (GCPs) were recorded using the Global Navigation Satellite System - Real Time Kinematic (GNSS-RTK) method. The GNSS-RTK method uses a network of widely spaced continuously operating base stations to give a positional correction to a user rover and a RTK network usually has at least one central processing station (Schloderer et al., 2010). The RTK network used in this study was the South African network of TrigNet base stations whose central processing station is located at the South African Chief Directorate: National Geospatial Information offices in Mowbray, Cape Town (Hedling et al., 2000). JAVAD Triumph-1M, a high precision 864 channel chip GNSS receiver was used for capturing the topographic GCP points. The International Terrestrial Reference Frame 2008 (ITRF2008) ellipsoidal height values were converted to orthometric heights by applying the South African GEOID 2010 separation model which is a closer approximation to the height above sea level (Chandler et al., 2010). Moreover, a horizontal shift from ITRF2008 WGS84 to the South African Hartesbeesthoek 1994 datum was applied to all captured points.

Two sets of GCPs were logged, namely, orthorectification points and accuracy assessment reference points. For the orthorectification points, markers were placed on the ground and surveyed for accurate georeferencing of the UAV derived orthomosaic as done in (Lucieer et al., 2012). The orthorectification data-set was used for georeferencing the UAV orthomosaic during the image matching stage of Structure from Motion (SfM) as applied in (Gini et al., 2013). It should be noted that orthorectification GCPs are not compulsory for SfM but the inclusion of orthorectification GCPs, camera extrinsic parameters (roll, pitch, yaw and geotags) and intrinsic parameters (tangential and radial lens distortion) increases the speed and accuracy of SfM image matching (Gini et al., 2013).

3.3.2. UAV flight planning and image mosaicking

This study made use of a customized UAV that has a net weight of 1.5 kg (excluding camera and batteries) and a payload of approximately 5 kg to acquire ultra-high spatial resolution UAV images (Figure 5). The fundamental components of the utilized UAV included a Global Navigation Satellite System (GNSS) receiver, an Inertial Measurement Unit (IMU) sensor and a barometer. The UAV was flown at a ground speed of 14 m/s at 160m above ground level (AGL). The camera mounted on the UAV was the Sony NEX-7, which has a Complementary Metal-Oxide Semiconductor (CMOS) imaging sensor. The Sony NEX-7 is a Mirrorless Interchangeable Lens Camera (MILC) whose sensor format is the

Advanced Photo System type-C (APS-C) CMOS. The camera exposure settings were set manually (as opposed to auto-exposure) so as to obtain equally focused images. The camera manual exposure program settings are shown in Table 7 and were established through a set of trial runs before being used in this study. The resultant single images had 6000 by 4000 pixels each with ground coverage of 234m by 156m.

Figure 7: Customized fixed wing UAV that was used to autonomously capture single geotagged images.

Table 7. Manual exposure program settings of the camera.

Exposure time	1/1000 sec.
ISO-speed	ISO-100
Focal length	15 mm
Maximum aperture	*f*/2.96875

Both co-located GCPs and the UAV imagery were captured on the 13 August 2015 and the 12 August 2016. The month of August in particular, is naturally known to be the late winter season in South Africa and thus regarded as the most appropriate phenological stage for mapping *H. pomanensis* (Mafanya et al., 2017). This is because the deciduous background vegetation shed leaves while *H. pomanensis* remains evergreen during this season. During image acquisition, the GNSS/IMU system on-board the UAV logged GPS co-ordinates of each captured image as events that were later used to geotag the raw images

using Ardupilot's open source Mission Planner (Osborne, 2016). The side and forward overlap were set to 60% and 80%, respectively. This image sampling redundancy is not only critical for providing a basis for checking scene illumination uniformity, as demonstrated in this study, but also for generating 3D point clouds, digital surface models (DSMs), and orthomosaics using UAV Structure from Motion (SfM).In particular, SfM is a photogrammetric 3D reconstruction technique that uses overlapping 2D images to create 3D point clouds, DSMs and orthomosaics. The SfM involves three stages of feature detection, image matching and bundle block adjustment (Wang et al., 2014). Furthermore, the proprietary Agisoft Photoscan (Agisoft LCC, 2018) software was used for image mosaicking using UAV-SfM. The geotagged raw images were administered into the Agisoft Photoscan photogrammetry package together with ten GCP points to produce georectified RGB orthomosaics as done in Coveney and Roberts (2017). The SfM does not require camera exterior orientations or interior orientations but the Agisoft lens software was used for lens distortion geometric calibration (Fraser et al., 2016). The ten GCPs were used to increase the mosaicking speed and image matching accuracy.

3.4. Vicarious radiometric calibration

3.4.1. Background

To have lasting quantitative value, it is standard practice to have remotely sensed data calibrated to physical units of reflectance (Smith and Milton, 1999). The radiometric calibration process converts image digital numbers (DNs) to at-surface reflectance units so as to enable quantitative analysis across data acquired at different seasons or times of the day as well as by different sensors. Calibrated datasets may be cross compared because while image DNs of a target object change depending on environmental factors such as the incoming irradiance and atmospheric conditions (Honkavaara et al. 2017), after radiometric calibration, the spectral characterization of an object becomes possible (Kelcey and Lucieer, 2012; Crusiol et al., 2017). Moreover, radiometric calibration improves the accuracy of derived vegetation indices as well as biochemical and biophysical parameters (Nguyen et al., 2015). In this regard, there are two mostly used radiometric calibration methods namely, (1) physical radiative transfer models which simulate the interaction of radiation with the atmosphere and the surface being remotely sensed and (2) vicarious empirical methods which predict relationships between radiance (usually recorded in DNs) and reflectance (ranging between 0-1). When there is no atmospheric variables measured at the time of image data acquisition,

vicarious empirical methods are often employed, especially when there is available *in situ* spectral data for calibration targets (Smith and Milton, 1999).

3.4.2. Calibration target design

For vicarious radiometric calibration, targets that are homogenous and resemble Lambertian properties are highly desirable (Del Pozo et al., 2014). While large homogenous natural targets are usually used for spaceborne radiometric calibration, use of artificial targets that are specifically designed for a project is usually made in UAV-RS. This is because coloured artificial targets are easy to transport to the field and can be easily moved to the next study area. Moreover, for the relatively smaller UAV-RS orthomosaics, compared to satellite RS scenes, it is often difficult to find naturally available pseudo-invariant features.

The types of materials used in UAV-RS radiometric calibration target design include plywood (Kelcey and Lucieer, 2012), Masonite hardboard (Wang and Myint, 2015), polyvinyl chloride (PVC) sheets and canvas (Del Pozo et al., 2014; Crusiol et al., 2017). For radiometric calibration target design, this study made use of the relatively affordable Masonite hardboards for the radiometric calibration target and a reinforced PVC sheet for the check target (Figure 6). The reinforced PVC check target with red, green, blue, black and white control colours was placed in the study area for accuracy assessment and error analysis.

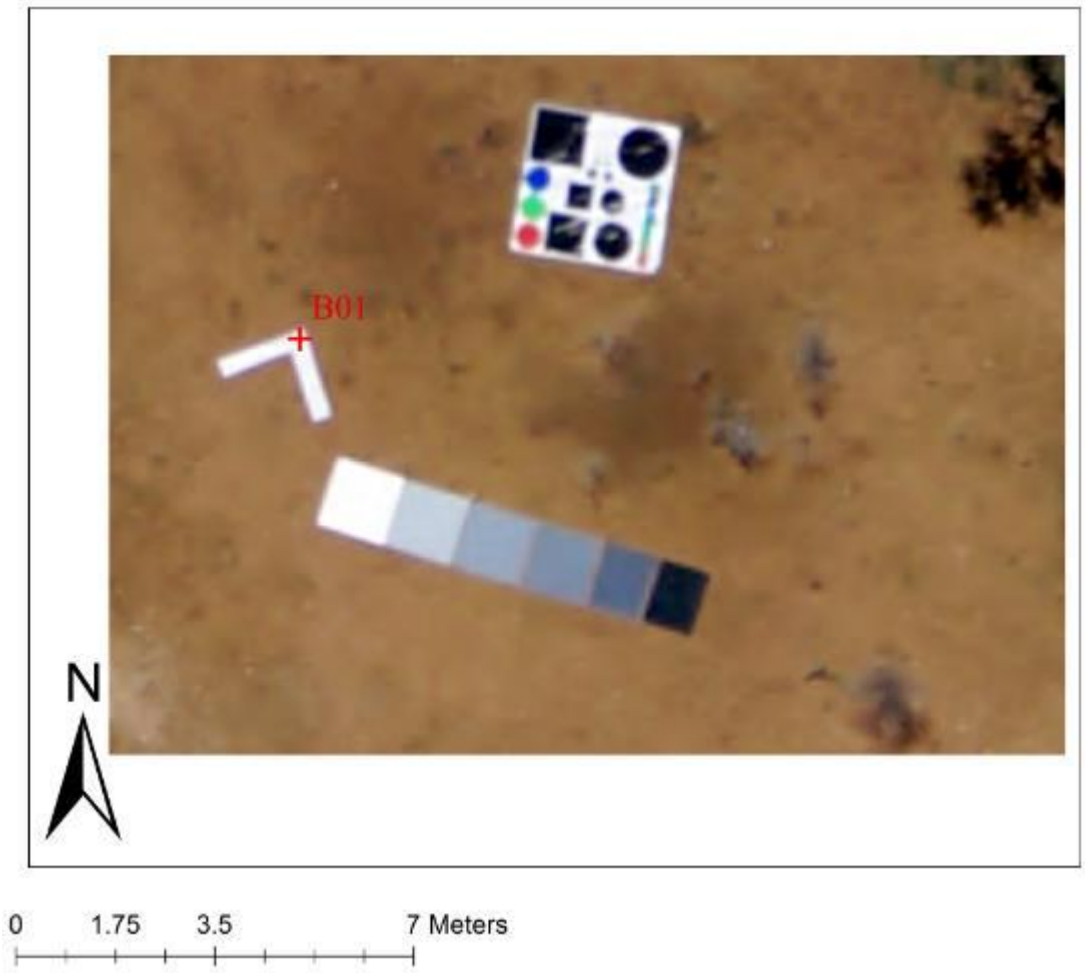

Figure 8: UAV aerial view of the control target (bottom) and check targets (top) taken by the Sony. Nex-7 camera on-board the UAV flown at a height of 160m AGL. The L-shaped marker in the middle (B01) was considered to be receiving similar irradiance as he radiometric calibration and check targets due to spatial proximity.

In particular, three standard size Masonite hardboards of 244cm x 122cm were painted with 1mm thick super white and black paints that were further mixed into four colour values of grey (totaling 6 calibration grey values). The calibration target was designed to form a grey gradient as follows; white, 20% grey, 40% grey, 60% grey, 80% grey and black. The mean spectral signature for each grey value is shown in Figure 7 which demonstrates the Lambertain properties of the created calibration target. The Lambertian properties of the grey gradient painted Masonite calibration target were first tested in a controlled room under an artificial light source and this material was found to be highly Lambertian in the visible region of the electromagnetic spectrum as also demonstrated by Wang and Myint (2015).

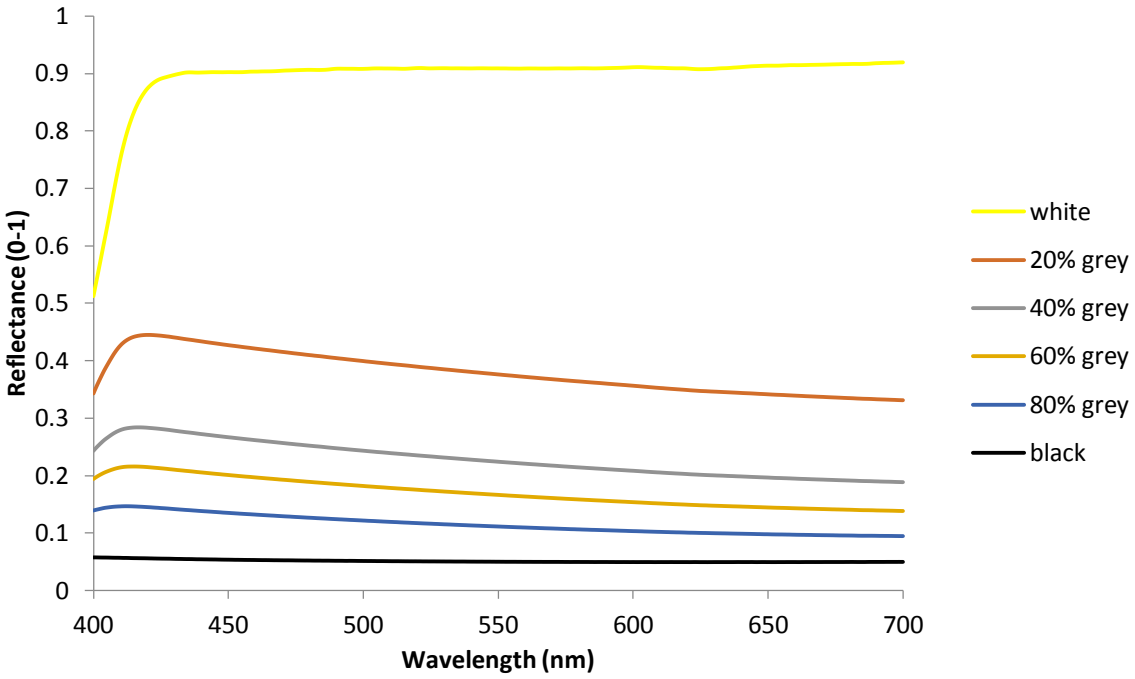

Figure 9: Mean spectral response curves of the Lambertian radiometric calibration targets. The white target (shown in yellow) has high reflectance while the black target has low reflectance.

Moreover, white PVC sheets were used to design L-shaped scene illumination uniformity check markers. The white PVC sheets were chosen to design the L-shaped markers due to ease of transportation and visibility in both raw images and the orthomosaic. The L-shaped PVC markers were placed randomly across the scene for orthorectification GCP surveying and the scene illumination uniformity check experiment. The calibration targets were placed in the study area before the UAV flight and the capturing of their spectral signatures was done before, during and after the UAV flight. This did not add significant time to the mapping process as the imagery was acquired at noon together with the spectral signatures. Also this was done so as to minimize the differences in solar illumination conditions between image data and *in situ* spectral signatures acquisition.

3.4.3. Scene illumination uniformity check

Intuitively, a large scale vicarious radiometric calibration method using radiometric calibration targets placed in only one region of the study area will require that the prevailing environmental conditions and solar illumination patterns (due to sun elevation angle) across the scene be uniform. To check if the environmental conditions and solar illumination

patterns are uniform across the scene, 10 L-shaped PVC markers were placed randomly, across the study area (Figure 8). The mean digital numbers (DNs) of the L-shaped markers, extracted from raw UAV images, were used to check if the illumination patterns and prevailing environmental conditions across the scene were the same during image data acquisition which took about 118 minutes. Due to the 60% side and 80% forward overlap photo sampling method employed in this study, each of the L-shaped markers appeared in at least 5 raw images. The ArcGIS 10.4 Spatial Analyst Zonal Statistics tool was used to extract the targets mean pixel DNs from a total of 58 raw images. The B01 marker was considered the reference illumination check maker because it was the closest marker to the radiometric calibration target. A two sample Student's t-test was conducted to check if the mean DN of the B01 marker, appearing in 6 images, was the same as the mean DNs of the rest of the 9 other markers that appeared in the remainder 52 images. This scene illumination uniformity check experiment was deemed necessary because, intuitively, mean reflectance values measured in only one spot within the scene should be used to calibrate the entire orthomosaic if and only the entire orthomosaic is experiencing similar atmospheric and illumination conditions.

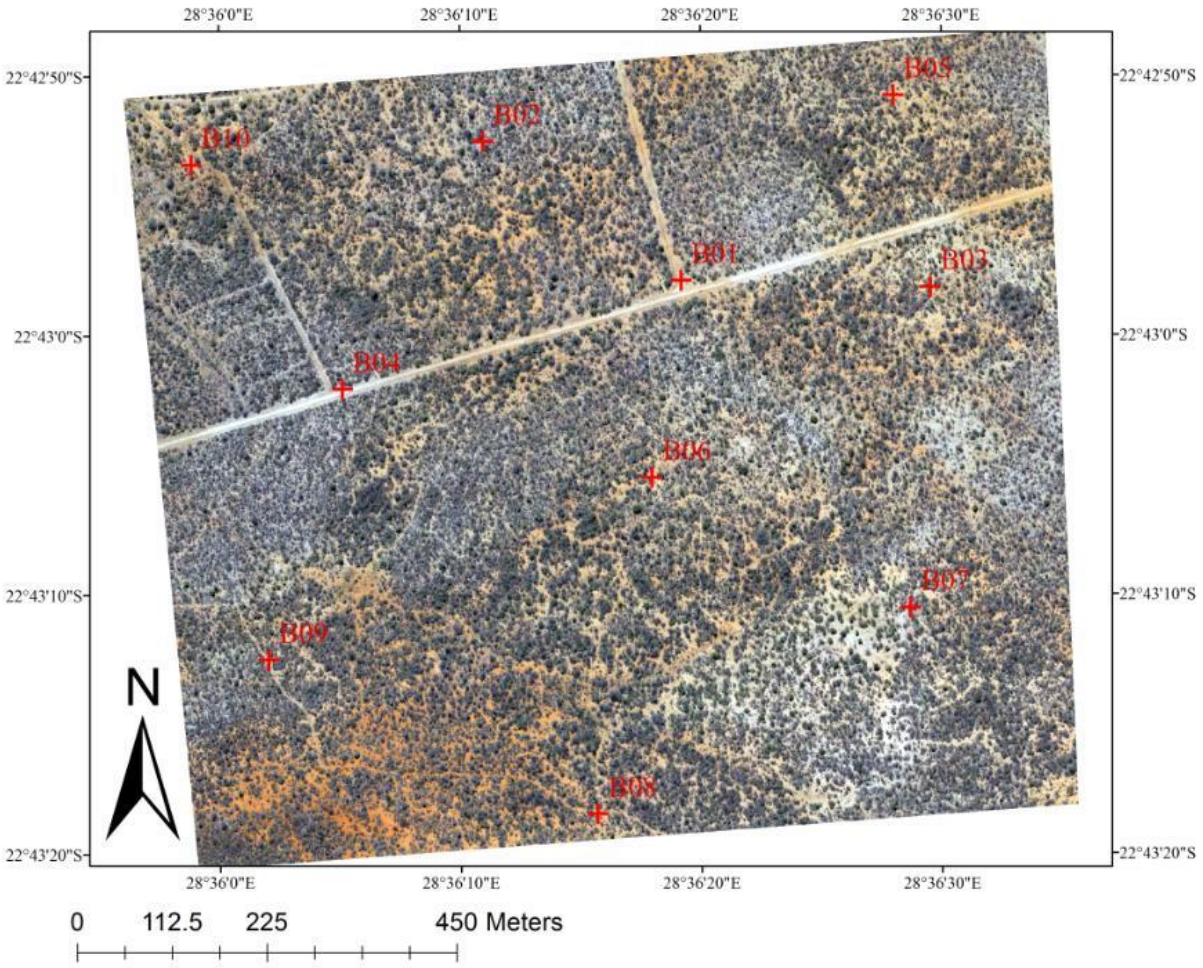

Figure 10: Mapped area showing the distribution of the 10 L-targets B01-B10. The target position is indicated by centers of the red crosses.

3.4.4. Empirical line method

Vicarious radiometric calibration procedures mainly focus on modelling the relationship between image DNs and *in situ* at-surface reflectance values of the calibration targets. In particular, the empirical line method is used to obtain image reflectance based on the measured spectral signatures of calibration targets that are placed on the ground (Hakala et al., 2010). The empirical line method (ELM) calibration prediction equations derived using mean target DNs and mean reflectance per waveband for each colour value of the calibration target were used in this study. The three equations were derived using mean DNs and mean reflectance values measured from a target located at a single spot of the study area. For *in situ* spectral measurements, the Analytical Spectral Devices, Inc. (ASD) FieldSpec 3 Pro calibrated spectroradiometer was used to take 25 spectral signatures (each spectra was a mean of 10 samples) for all the six grey values of the calibration target. An average of the 25

spectra was taken for each grey value thus totaling 250 individual measured spectral signatures for each grey value.

To obtain a single *in situ* at-surface reflectance measurement for each grey value on the calibration target, the 1nm spectral measurements were averaged according to the spectral response curve of the Sony NEX-7 CMOS sensor. Berra et al. (2015) measured the spectral sensitivity of the Sony CMOS using a monochromatic light source and the relative colour channels of the Sony CMOS were found to be approximately 400nm-490nm, 491nm-590nm, and 591nm-690nm for the blue, green and red colour channels, respectively. The same method was followed to get mean spectral signatures for the coloured PVC check targets. To obtain the mean image DN for each grey value of the calibration target, use of the Zonal Statistics tool within the ArcGIS 10.4 Spatial Analyst extension was made. Considerable care was taken to create polygons that contain only pixels that belong only to that particular grey value.

In most studies, a linear relation between image DNs and the at-surface reflectance values is assumed (Karpouzli and Mathus, 2003). When more than two calibration targets are used, the relationship between image DN and reflectance does not have to be assumed to be linear (Smith and Milton, 1999). In this study, the mean DN were regressed with the mean reflectance values and the relationship between image DN and reflectance was found to be exponential for all the three image wavebands as also observed in Wang and Myint (2015). Following the simplified empirical line method proposed by Wang and Myint (2015), a natural log transformation was performed on all the six mean *in situ* at-surface spectra for each image waveband. The transformation showed that a linear relationship exists between mean image DNs and the mean natural log-transformed spectral values for each waveband. When the y-intercept of the linear equation is converted back to reflectance, the result is a minimum at-surface reflectance value for that particular image waveband. Therefore, the y-intercept of each waveband is the constant radiometric calibration parameter for that particular waveband. Moreover, the y-intercept co-ordinates can be used as an initial point in a Cartesian plane. To derive an ELM prediction equation, another point in the Cartesian co-ordinate system can be represented by the mean DN and mean at-surface reflectance of the entire calibration target for each image waveband. These two points can then be used to calculate the gradient (m) of the calibration equation. The gradient is given by equation (1) below;

$$m = \frac{B_y - A_y}{B_x} \quad (1)$$

where A_y is the constant radiometric calibration parameter,B_x the mean DN of the calibration target, and B_y the natural log-transformed mean reflectance of the calibration target (Wang and Myint, 2015). The developed ELM prediction equations were used to convert each waveband of the orthomosaic from DNs to reflectance values using the raster calculator in QGIS (Quantum GIS development team, 2018). Subsequently, the three image wavebands were stacked together to give a colour RGB image with reflectance values instead of DNs. The radiometric calibration using the raster calculator in QGIS took about half an hour and therefore did not delay the mapping process.

3.4.5. Radiometric calibration accuracy assessment

The mean spectra of the PVC check target with black, blue, green, red and white colours was used for accuracy assessment. During the acquisition of the *in situ* validation data, 5 spectra (a total of 50 individual spectral signatures) were measured for each check colour. The Zonal Statistics tool in ArcGIS 10.4 was used to get the mean reflectance of each coloured check target for each waveband. There were 6 available mean reflectance values for each coloured check target (i.e. 1 estimated and 1 measured mean value for each waveband thus totalling 24 values).The estimated image mean reflectance values and mean reflectance *in situ* measurements for each coloured target circle or square were then correlated so as to validate the large scale radiometric calibration method used in this study. Error analysis through Root Mean Square Error computations was used to supplement the correlation analysis.

3.5. Image classification

3.5.1. Background

The developments in UAV technology have afforded the remote sensing community the opportunity to map the environment at enhanced spatial resolutions. Use of consumer grade digital cameras with ultra-high spatial (<5m) but low spectral resolution (~100nm) in UAV-RS is often used due to the limited payload capacity on these systems (< 50kg) (Laliberte et al., 2011). For example, in the Czech Republic, Dvořák et al. (2015) developed a rapid, repeatable and efficient UAV based method for the mapping and monitoring of IAPs

from consumer grade digital cameras. Use of UAVs for producing high spatial resolution datasets has several advantages over the manned aircraft or spaceborne platforms for accurately mapping IAPs and these include flexible temporal resolution and low data acquisition costs (Dvořák et al., 2015). The high spatial resolution can be attributed to the fact that UAV systems allow for data acquisition at low flight altitudes of usually less than 150m above ground level (Cracknell, 2017). The effect of high spatial resolution was demonstrated in Wan et al., (2015) whereby a 94% overall accuracy for mapping IAPs was obtained using 80cm UAV-derived imagery. Furthermore, frequent IAPs monitoring efforts based on remotely sensed imagery may require development of semi-automatic image classification systems that are able to map, quantify and monitor the presence of IAPs (Peerbhay et al., 2016).

Supervised or unsupervised (pixel-based, object-based and hybrid) classification approaches have been tested for mapping IAPs (Dvořák et al. 2015). In particular, iterative semi-automated object based classification approaches have been used to map IAPs such as *Heracleum mantegazzianum (*Giant hogweed) from ultra-high spatial resolution UAV-derived data (Müllerová et al., 2016). For high resolution imagery, the object-based image classification techniques have demonstrated improved performance over the pixel based approach (Chen et al., 2014). The first and critical step in object-based image classification is segmentation which encompasses grouping of similar pixels, according to some similarity threshold, into homogenous objects (Liu et al., 2012). The object-based image analysis (OBIA) techniques do not only allow for the consideration of spectral information but also contextual, textural, shape and spatial relationships in image objects as opposed to single pixels (Sebari and He, 2013).

This study compared five image classifiers using two different interlinked evaluation strategies. The evaluation strategies used were point and area based accuracy assessment. The compared classifiers were unsupervised pixel based classifiers (*k-mediuns* and *Euclidian Length*), unsupervised object based classifier (*Isoseg*), supervised pixel based classifier (*Maxver*) and supervised object based classifier (*Bhattacharya*). The image classification for this study was done in Spring open source software (Camara et al., 1996).

3.5.2. Description of the utilized image classifiers

Five image classifiers were chosen and evaluated in order to determine the classifier with the lowest omission and commission errors for mapping *H. pomanensis* from the UAV derived orthomosaic. The image classifiers used were the unsupervised pixel based (*K-*

mediuns and *Euclidian length*), unsupervised object based (*Isoseg*), supervised pixel based (*Maxver*) and the supervised object based image classifier (*Bhattacharya*).

In particular, the *K-mediuns* classifier considers the median vector of a pixel and assigns the pixel to a class with the closest class median vector according to a similarity threshold. The comparison and pixel assignation of *K-mediuns* could be regarded as reliable because the median is known to be less affected by outliers than the mean. On the other hand, the *Euclidian length* classifier uses an algorithm that calculates the Euclidean distance between a pixel spectral mean vector and a class mean vector and then assign the pixel to the class of shortest distance according to a similarity threshold (Wang et al., 2005). In this study, the two aforementioned classifiers were used to generate 16 unsupervised classes that were later grouped into four land cover classes (ground, conifers, deciduous trees and *H. pomanensis*). These classes were regarded as the general land cover types available in the study area.

The *Maxver* classifier uses the Maximum Likelihood (ML) algorithm which assumes that the digital numbers of a class in the image bands are normally distributed and calculates the probability of each pixel belonging to that class (Yang et al., 2011). The ML takes into account the mean and covariance vectors of the training sets of a class in a 3-dimensional space and assigns each pixel to the class for which it has the highest probability of membership (Silva et al., 2013). Since the *Maxver* classifier is a supervised classification technique, all pixels were assigned to the four land cover classes, accordingly. The classes were created during the training stage of image classification. The training involved creating polygons or areas that contain only the class of concern.

While the pixel based image classifiers described above assign pixels to classes, the object based image classifiers (i.e. *Isoseg* and *Bhattacharya*) classify objects or segments instead of pixels. This means that image segmentation is the first step in object based image classification and partitions the image into objects by grouping associated pixels together using a similarity threshold. The partitioning of the remotely sensed image into segments is important because images contain not only spectral information but also structural parameters such as texture, spatial pattern, size and shape information which are neglected in pixel based image classification techniques (Blaschke and Strobl, 2001). In this study, the UAV orthomosaic was segmented using the *region growing* technique. After some trial runs, a grouping of 350 pixels with 6 similarities was found to be good parameters for partitioning the UAV derived RGB orthomosaic used in this study as this grouping provided large enough but non class mixing objects. This is important because too small segments take longer to

process while training with class mixing segments during training results in commission errors.

Furthermore, the *Isoseg* classifier assigns segments to a class using the Mahalanobis distance which is the dissimilarity measure between a segment mean vector *x* and a class mean vector *y* of the same probability distribution with covariance (De Maesschalck et al.,2000). The *Isoseg* classifier makes use of the K-means clustering algorithm to assign a particular segment to a certain class. A 3-dimensional decision surface, which is a hyperellipsoid, is created for each class and this surface has a mean vector (i.e. the mean vector of the class). The K-means algorithm uses the mean vector of the class in question as an initial centre and then all segments whose means fall inside this class's hyperellipsoid are assigned to that particular class. This is because such segments meet the criteria according to the analyst specified Chi-square acceptable threshold percentage (Duda and Hart, 1973). The analyst then merges similar together (Filho et al., 1997). The 16 generated classes were then merged into the four land cover classes under consideration in this study.

The *Bhattacharya* classifier, on the other hand, uses the Bhattacharya distance which measures the similarity of probability distribution curves between a candidate segment and a class (Choi and Lee, 2003). The Bhattacharya distance is the distance between the centres (i.e. means) of those two probability distributions. Segments that are closely inside a particular class's distribution threshold compared to other classes are assigned to that particular class (Camara et al., 1996). Since the *Bhattacharya* classifier is a supervised image classification technique, all segments were assigned to the predefined four land cover classes. The classes were created during the training stage of image classification.

3.6. Accuracy assessment

3.6.1. Point based accuracy assessment

For each of the 5 classifiers, 3 error matrices were generated based on the (i) GNSS-RTK points (N_1=119), (ii) independently-derived random points (N_2=100) and (iii) combined set of reference points (N_3 =219) across the ground, conifers, deciduous trees and *H. pomanensis* land cover types. In addition, the overall accuracy and the estimate of Kappa were used to compare classification results of the 5 image classifiers from 15 error matrices across the aforementioned land cover types. Equations (2)-(4) and (7) (Table 8) were used to calculate the overall accuracy ($p_o\mathrm{X}$), chance agreement ($p_c\mathrm{X}$), Kappa estimate ($\hat{\mathrm{k}}_{\mathrm{X}}$) and the

variance of the Kappa estimate ($\text{var\_}\hat{k}_X$), respectively. Furthermore, Equations (5) and (6) in (Table 8) represent parameters for the computation of the variance $\hat{k}$ (Lentilucci, 2006).

Table 8: Expressions used for calculating the overall accuracy, chance agreement, estimate of Kappa and its variance.

Equation and statistic name
$p_o X = \frac{1}{N_X} . \sum_{i=1}^{n} p_{ii}(X)$ Overall accuracy (2)
$p_c X = \frac{1}{N^2{}_X} . \sum_{i=1}^{n} RT(X)^{<i>} . CT(X)^{<i>}$ Chance agreement (Lentilucci, 2006) (3)
$\hat{k}_X = \frac{p_o X - p_c X}{1 - p_c X}$ Kappa estimate (Lentilucci, 2006) (4)
$a_{1x} = \sum \left[\frac{1}{N_x{}^2} . \sum_{i=1}^{n} X_{i,i} . (RT_{(X)}{}^{<i>} + CT_{(X)}{}^{<i>}) \right]$ (5)
$a_{2X} = \sum \left[\frac{1}{N_X{}^3} . \sum_{i=1}^{n} \sum_{j=1}^{n} X_{i,j} . (RT_{(X)}{}^{<i>} + CT_{(X)}{}^{<j>})^2 \right]$ (6)
$\text{var\_}\hat{k}_X = \frac{1}{N_X} . \left[\frac{p_o X . (1 - p_o X)}{(1 - p_c X)^2} + \frac{2 . (1 - p_o X)(2 . p_o X . p_c X - a_{1X})}{(1 - p_c X)^3} + \frac{(1 - p_o X)^2 . (a_{2X} - 4 . p_c X^2)}{(1 - p_c X)^4} \right]$ Variance of the Kappa estimate (Lentilucci, 2006) (7)

Where;

- X is the error matrix of either *K-mediuns*, *Euclidian length*, *Isoseg*, *Maxver* or *Bhattacharya* classifier,
- N_X = the total number of reference points,

- n =4 (i.e. the number of classes viz. Ground, Conifers, Decidous and *H. pomanensis*),
- P_{ii} = the number of correct observations for the *i*th class,
- $\mathrm{RT}(\mathrm{X})^{<i>}$ or $\mathrm{RT}_{(\mathrm{X})}{}^{<i>}$ = Row Total of the *i*th class,
- $\mathrm{CT}(\mathrm{X})^{<i>}$ or $\mathrm{CT}_{(\mathrm{X})}{}^{<j>}$ = Column Total of the *i*th or *j*th class,
- $p_o\mathrm{X}$ = Overall accuracy,
- $p_c\mathrm{X}$ = Chance agreement,
- $\hat{\mathrm{k}}_{\mathrm{X}}$ = Kappa estimate,
- $\mathrm{a}_{1\mathrm{x}}$ and $\mathrm{a}_{2\mathrm{X}}$ are parameters used in the calculation of the variance, and
- var_$\hat{\mathrm{k}}_{\mathrm{X}}$ = Variance of the Kappa estimate (Lentilucci, 2006; Senseman et al., 1995)

3.6.2. Hypothesis testing for point based accuracy assessment

In this study, a statistical hypothesis test was conducted to determine whether the difference between the Kappa values of accuracy assessment results of two classifiers is significant (Congalton, 1991). In other words, the test was conducted to determine whether the image classifier with the highest Kappa value produced better classification results, than the image classifier with the second highest Kappa value. Given the large sample size (i.e. N ≥30) of reference data points used in this study for accuracy assessment, the Z-test was applied when conducting the hypothesis test between the Kappa estimates of the two best performing image classifiers. Therefore, the null and alternative hypotheses were formulated as follows;

$$\mathrm{H}_0 : \left[\hat{\mathrm{k}}_{\mathrm{X}} - \hat{\mathrm{k}}_{\mathrm{Y}} \right] = 0 \qquad (8)$$

$$\mathrm{H}_1 : \left[\hat{\mathrm{k}}_{\mathrm{X}} - \hat{\mathrm{k}}_{\mathrm{Y}} \right] > 0 \qquad (9)$$

where, H_0 denotes the null hypothesis that there is no difference between the classification accuracy results of image classifiers X and Y. $\hat{\mathrm{k}}_{\mathrm{X}}$ and $\hat{\mathrm{k}}_{\mathrm{Y}}$ denote the Kappa estimates of image classifier X and Y, respectively and H_1 denotes the alternative hypothesis that the classification accuracy results of image classifier X are significantly greater than those of classifier Y. According to Congalton (1983), the Z-test statistic for determining whether image classifier X produced better classification results than image classifier Y can be calculated as follows;

$$Z_{XY} = \frac{\hat{k}_X - \hat{k}_Y}{\sqrt{var\_\hat{k}_X + var\_\hat{k}_Y}} \quad (10)$$

where, Z_{XY} is the standard normal deviate. Here, H_0 we can be rejected at 95% confidence interval given that $Z_{XY} \geq 1.96$ (Congalton, 1991). However, if $Z_{XY} < 1.96$, we cannot reject H_0 which asserts that the classification results of image classifier X and Y are possibly not different, which means that image classifier X did not produce better classification results than image classifier Y.

3.6.3. Area based accuracy assessment: Comparison of areal estimates between the Maxver and Bhattacharya classifiers.

For the area based accuracy assessment, a set of 35 polygons was created through visually interpreting and hand digitising clumps of *H. pomanensis* that varied from about 4m^2 to about 60m^2 on the UAV RGB orthomosaic. During creation of the polygons, care was taken to digitize homogenous pixels that comprise of *H. pomanensis*, while disregarding visible spaces of ground and/or other surrounding land cover types. Thus, the aforementioned polygons were considered as independently-derived reference data for area based accuracy assessment in this study. The polygons were used to compute areal estimates of *H. pomanensis* and compare them to the areal estimates mapped by the *Maxver* and *Bhattacharya* classifiers within those polygons. Furthermore, the polygons were used to quantify omission errors in the classification maps followed by the qualitative assessment of commission errors.

3.6.4. Comparison of the radiometric calibrated and uncalibrated orthomosaics for the best classifier.

This study also determined whether radiometric calibration increased mapping accuracy. In particular, the 97ha UAV-derived orthomosaic was divided into 9 tiles as shown in Figure 9. The centre tile was used to compare the accuracy assessment of the best performing image classifier by applying it to both calibrated and and uncalibrated centre tiles. A 3 by 3 matrix was used to tile both calibrated and calibrated orthomosaics into 9 tiles, namely, A1, A2, A3, B1, B2, B3, C1, C2 and C3. For accuracy assessment, a total of 200 (N_4=200) random points was generated for the entire 97ha orthomosaic. Of the 200 random

points, only 21 (N_5=21) points fell within the centre tile B2 as shown in Figure 10. Error/confusion matrices were then created for the N_5 points.

A1	A2	A3
B1	B2	B3
C1	C2	C3

Figure 11: A 3 by 3 matrix used to divide the 97ha orthomosaic into 9 tiles. The highlight B2 tile was used to determine whether radiometric calibration increases mapping accuracy.

Figure 12: View of the centre tile B2 with 21 randomly generated accuracy assessment points.

CHAPTER 4

RESULTS

4.1. Camera calibration analysis

The intrinsic camera parameters (i.e. tangential and radial distortions) are required for the geometric calibration of non-metric cameras that are widely used in UAV-RS. In particular, these parameters are not used to physically adjust the camera lens but are incorporated in SfM mosaicking for faster and more accurate image matching. In this study, the camera interior orientation data was imported from Agisoft Lens so that Agisoft Photoscan (i.e. the SfM mosaicking software) can take them into account during image mosaicking (Figure 11). The camera radial distortion curve of the non-metric camera example used was less smooth than the tangential distortion curve and as a result this could be attributed to the short range from which the LCD screen images were taken.

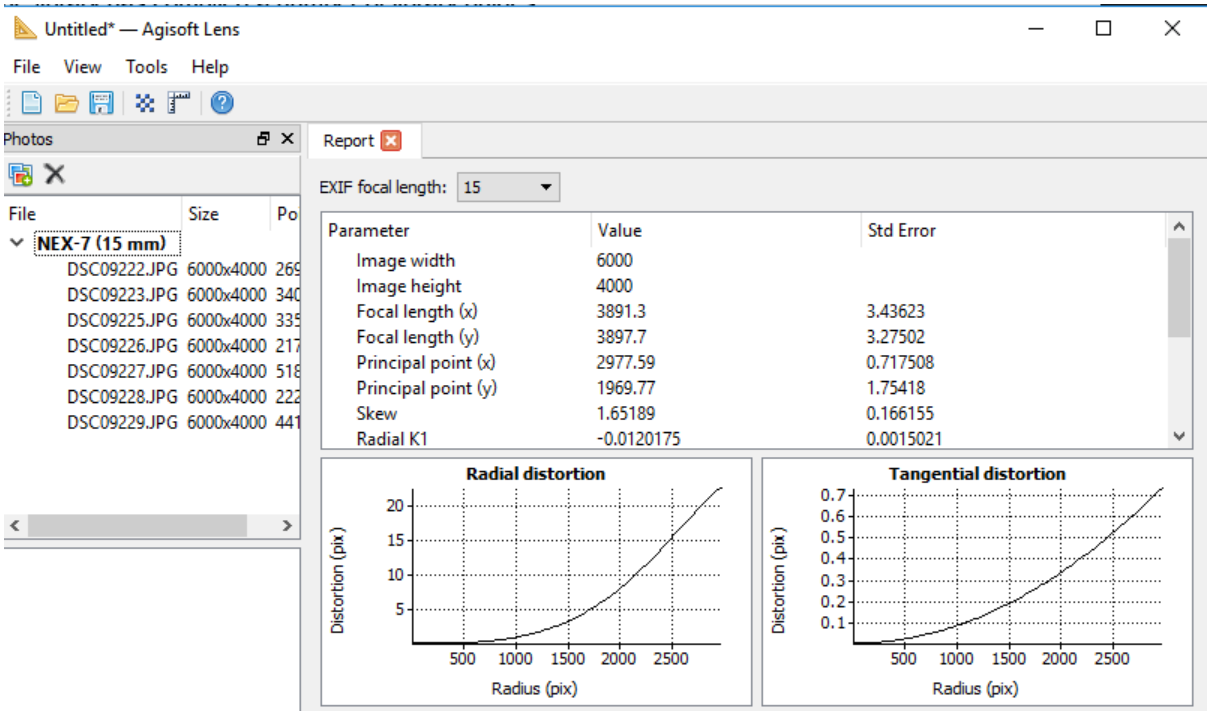

Figure 13: Geometric camera calibration parameters from Agisoft Lens showing the intrinsic radial and tangential distortions

4.2. Analysis of the radiometric calibration

The descriptive statistics shown in Table 9 were used in a two sample Student's *t*-test that was performed between the mean DN of the reference illumination uniformity check marker (B01) and the other L-shaped markers (B2-B10). In particular, the results in Table 9 reveal that the reference L-shaped marker (B01) had higher variance, standard deviation and mean pixel DNs when compared to the combined L-shaped markers (B2-B10). This could be attributed to the fact that B01 appeared in only 6 raw images while the combined number of images in which the other markers (B2-B10) appeared in is 52. However, the difference of 1.36 between the mean DNs in Table 9 was not found to be statistically significant at the 95% confidence interval ($p<0.05$). This information suggests that it is justifiable to calibrate the entire orthomosaic using radiometric calibration equations derived from mean reflectance values measured in one spot only within the 97ha RGB orthomosaic. These results further suggest that the entire scene mapped was experiencing similar atmospheric and illumination conditions.

Table 9: Descriptive statistics for reference uniformity check L-shaped markers.

Statistic	B01 Marker	B02-B10 Markers
Mean DN	223.98	222.62
Variance of DNs	34.63	28.63
STD deviation of DNs	5.88	5.35

The scene illumination uniformity inference allowed for the radiometric calibration of the entire scene using parameters derived from radiometric calibration targets placed in only one spot within the study area using ELM. Reportedly, vicarious radiometric calibration procedures mainly focus on modelling the relationship between image DNs and *in situ* at-surface reflectance values of the calibration targets (Smith and Milton, 1999). A summary of the regression relationships between image DNs and *in situ* reflectance measurements in the red, green and blue wavebands is presented in Table 10. The regression equations (11)-(13) in Table 10 show that the relationship between image DNs and *in situ* reflectance measurements in all the camera wavebands is exponential. An exemplary visual depiction of the exponential relationship for the red waveband is shown in Figure 12.

Table 10: Summary of regression relationships for each waveband

	Red band	Green band	Blue band
Regression equation	$y = 0.032e^{(0.014DN)}$ (11)	$y = 0.032e^{(0.013DN)}$ (12)	$y = 0.029e^{(0.013DN)}$ (13)
Coefficient of determination	$R^2 = 0.99\ (p < 0.01)$ (14)	$R^2 = 0.99(p < 0.01)$ (15)	$R^2 = 0.98\ (p < 0.01)$ (16)
ln(refl.)	$Y = -0.014x + 3.423$ (17)	$Y = -0.013x + 3.434$ (18)	$Y = -0.013x + 3.518$ (19)

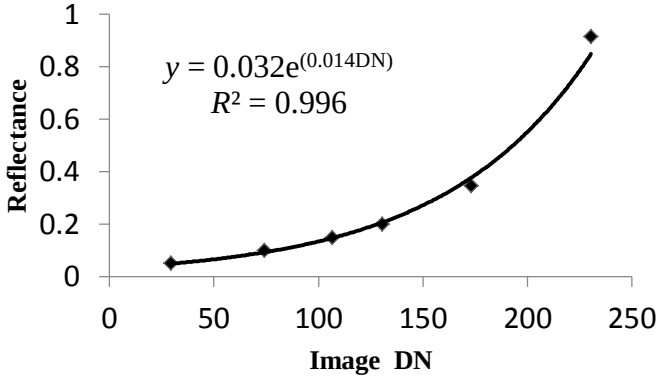

Figure 14: Example of the relationship between image digital numbers and *in situ* at-surface reflectance values for the Red waveband.

Furthermore, Figure 13 shows that there exists a linear relationship between the natural log transformed reflectance values and image DNs. A similar observation was made in Wang and Myint (2015). This relationship is such that the y-intercept 3.423 (Figure 13 and Equation 18 in Table 10) can be converted to reflectance (i.e. $e^{-3.423}$ = 0.0326) which represents the minimum at-surface reflectance value that the Sony Nex-7 CMOS sensor used in this study can detect in the red waveband colour channel. In addition, the utilised CMOS sensor can detect minimum at-surface reflectance values of 0.0322 and 0.0296 for the green and blue wavebands, respectively. The minimum at-surface reflectance values for the green and blue wavebands were derived using the y-intercepts (i.e. the calibration constant parameters) in equations (19) and (20), Table 10.

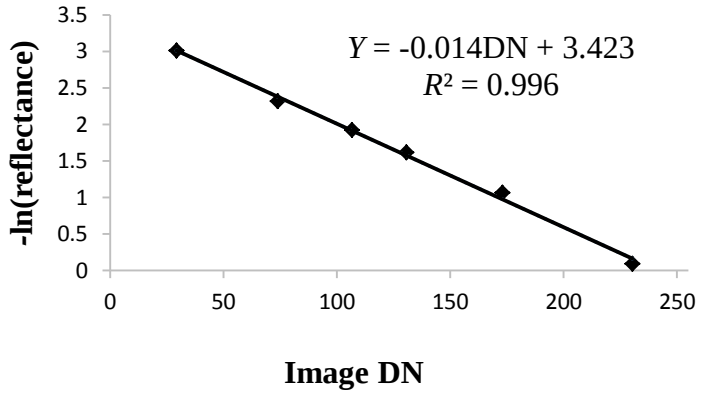

Figure 15: Example of the relationship between natural log-transformed reflectance and *in situ* at-surface reflectance values for the Red waveband.

To derive the radiometric calibration equations, let the the y-intercept value for each transformed exponential equation (i.e. the linear equations (21)-(23)) represent the constant calibration parameter in the empirical line calibration equation of type,

$$-ln(reflectance) = m\ x\ DN + C \qquad (20)$$

where the gradients of each image waveband replace *m* in the derived radiometric calibration equations (Table 11). The derived linear equations (21)-(23) in Table 11 were used to calibrate the raw 97ha RGB orthomosaic image wavebands. Subsequent layer stacking, quantitative analysis and accuracy assessment were thus performed on the calibrated orthomosaic.

Table 11: Linear radiometric calibration equations for the red, green and blue wavebands.

Image waveband	Radiometric calibration equation
red	$-ln(reflectance) = -0.01413xDN + 3.423$ (21)
green	$-ln(reflectance) = -0.01385xDN + 3.434$ (22)
blue	$-ln(reflectance) = -0.01338xDN + 3.518$ (23)

To validate the proposed vicarious radiometric calibration method, reflectance values derived from the calibrated image wavebands were regressed against *in-situ* measured reflectance values for the check targets. Results shown in Table 12 present the comparison

between mean reflectance values derived from the calibrated image wavebands (Estimated) and their respective *in situ* at-surface reflectance values (Measured) for the black, blue, green, red and white check targets. There are three data points for each check target representing each waveband. The regression between the reflectance values derived from the calibrated image wavebands and the measured at-surface reflectance values resulted in a correlation coefficient r value of 0.977 ($p<0.01$) as shown in Figure 15. Furthermore, the Root Mean Square Error (RMSE) between estimated and measured reflectance values in Table 12 (i.e. for all the three wavebands and five check targets) was found to be 0.063 whereas the waveband specific RMSE values were 0.040, 0.048 and 0.089 for the red, green and blue image wavebands, respectively. The aforementioned strong correlation coupled with the low overall RMSE values suggest low discrepancies between the *in situ* measured mean reflectance values and the reflectance values derived from the radiometric calibrated image wavebands. In particular, the highest RMSE value of 0.089 reported for the blue waveband could be attributed to the fact that scattering of radiation by the atmosphere is greater at shorter wavelengths (Smith and Milton, 1999). Hence the *in situ* proximally sensed white target mean reflectance of 0.815857 is much higher than the remotely sensed mean reflectance of 0.658850 in the blue waveband colour channel of the Sony Nex-7 camera. This is because proximal sensing was done at 1m above the check targets while remotely sensed images were taken at 160m AGL, meaning radiation interacted with more atmospheric particles in the latter case. In overall, these error analysis and the strong correlation results validate the proposed radiometric calibration framework for applications in semi-arid woodlands.

Table 12: Comparison between check targets (black, blue, green, red and white) mean reflectance values and their respective *in situ* at-surface reflectance values.

		Estimated	**Measured**
Black square	**Red**	0.046607	0.054228
	Green	0.044089	0.049955
	Blue	0.041845	0.047642
Blue Circle	**Red**	0.046601	0.026515
	Green	0.062312	0.066245
	Blue	0.361492	0.241355
Green Circle	**Red**	0.088030	0.150555
	Green	0.447994	0.362182
	Blue	0.132574	0.110585
Red Circle	**Red**	0.557448	0.521022
	Green	0.070380	0.070882
	Blue	0.074535	0.053538
White Square	**Red**	0.709671	0.759841
	Green	0.717760	0.782323
	Blue	0.658850	0.815857

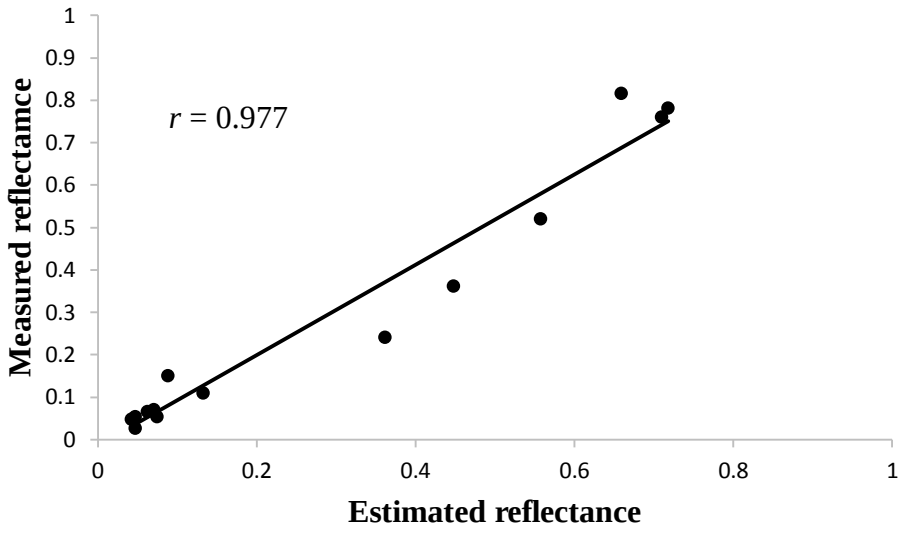

Figure 16: Regression between *in situ* measured reflectance and the reflectance values derived from the calibrated image wavebands (r = 0.977).

4.3. Image classification analysis and accuracy assessment

Point and area based accuracy assessments were utilised to determine the best performing classifier for mapping *H. pomanensis.* In particular, point based accuracy assessment results of the five evaluated image classifiers for mapping *H. pomanensis* are presented in Tables 13-15. Results based on the GNSS-RTK reference points (N_1=119) showed that the *Maxver* and *Bhattacharya* classifiers had higher producer accuracies of 83.7% and 95.1% than the unsupervised classifiers, respectively (Table 13). This indicates that the aforementioned supervised classifiers provide better mapping of *H. pomanensis* with low omission errors of 16.3% and 4.9%, respectively. Furthermore, while virtually similar mapping performance with regard to the user accuracies of all classifiers is observed (Table 13), the unsupervised *K-mediuns* classifier had the highest user accuracy that is analogous to 0% commission error. Overall, the *Maxver* and *Bhattacharya* supervised classifiers had the highest overall accuracies of about 90 % with corresponding $\hat{k}$ values of 0.86 and 0.88 respectively (Mafanya et al., 2017).

Table 13: Accuracy assessment of the five image classifiers for mapping *H. pomanensis* based on the GNSS-RTK reference points (N_1 = 119).

Classification type:		**Classifier**	**Producer Accuracy (%)**	**User Accuracy (%)**	**Overall Accuracy %**	$\hat{k}$
Unsupervised	Pixel based	*K-mediuns*	48.8	100	67.2	0.57
		Euclidian Length	65	79	75	0.66
	Object based	*Isoseg*	38.8	79.2	57.1	0.41
Supervised	Pixel based	*Maxver*	83.7	87.8	89.9	0.86
	Object based	*Bhattacharya*	95.1	90.7	89.9	0.88

Other accuracy assessment results based on the set of independently-derived random reference points (N_2 =100) are presented in Table 14. A good mapping accuracy of the *Maxver* and *Bhattacharya* supervised classifiers is evident (Table 14) corroborating results in Table 13. In particular, these two classifiers had overall accuracies and kappa values above 0.80 notwithstanding their notable relative performance in the producer and user accuracies, respectively. On the other hand, the unsupervised *Euclidian length* classifier yielded the highest producer accuracy of 94% (compared to all other classifiers) coupled with 75% overall accuracy. Furthermore, the overall accuracies of the *K-mediuns* and *Isoseg* unsupervised classifiers showed an inadequate classification.

Table 14: Accuracy assessment of the five classifiers detecting *H. pomanensis* based on the N_2 =100 independently-derived reference points.

Classification type:		**Classifier**	**Producer Accuracy (%)**	**User Accuracy (%)**	**Overall Accuracy (%)**	$\hat{k}$
Unsupervised	Pixel based	*K-mediuns*	25	18.2	67	0.46
		Euclidian Length	93.8	48.4	75	0.64

	Object based	*Isoseg*	12.5	14.3	64	0.36
	Pixel based	*Maxver*	75	66.7	85	0.82
Supervised	Object based	*Bhattacharya*	85.7	100	81.0	0.68

Furthermore, Table 15 presents another set of accuracy assessment results based on a combined data-set of reference points (N_3=219). This set of results gave an indication of consistency in the mapping performance of all five classifiers across all three assessments (Tables 13-15). In particular, the supervised classifiers depict optimal overall accuracy above 80% in all three assessments compared to unsupervised classifiers (Tables 13-15). Additionally, the results show that the *Maxver* and *Bhattacharya* supervised classifiers can be expected to map *H. pomanensis* with relatively low omission errors of 17.6% and 10% and commission errors of 16% and 4.3%, respectively (Table 15). Such mapping performance was followed by the unsupervised *Euclidian length* classifier with omission error of 27.4% and commission error of 35.7% (Table 15). Thus the best two performing classifiers (*Maxver* and *Bhattacharya*) were further evaluated using error matrices in Table 16 and 17 below.

Table 15: Accuracy assessment of the five classifiers for detecting *Harrisia pomanensis* based on the N_3=219 reference points.

***Harrisia pomanensis* classification accuracy assessment**				**Percent Accuracy**			
Classification type:		Classifier	Estimated Area (m^2)	Producer	User	Overall	$\hat{k}$
Unsupervised	Pixel based	*K-mediuns*	77964.8	42.3	78.6	67.1	0.49
		Euclidian Length	249309.2	72.6	64.3	74.9	0.66
	Object based	*Isoseg*	62676.0	35.1	64.5	60.3	0.46
Supervised	Pixel based	*Maxver*	84604.7	82.4	84	87.7	0.83
	Object based	*Bhattacharya*	59960.0	90.0	95.7	85.8	0.81

Results of the point based accuracy assessment for the best two performing classifiers using the combined reference data (N_3=219) showed that the *Maxver* classifier had user and producer accuracies greater than 82% across all land cover types (Table 16). The *Bhattacharya* classifier on the other hand had the highest producer accuracies (i.e. lowest omission errors) than the *Maxver* except for the deciduous trees land cover class (Table 17). Furthermore, the *Bhattacharya* classifier had user accuracies above 94% for all land cover type classes, except for the ground class, whereas the commission and omission errors of the *Maxver* classifier were similar across all land cover type classes (Table 17).

Table 16: Point based accuracy assessment of Maxver classifier error matrix using combined reference data (N_3 =219) across all land cover type classes.

	Class	**Ground**	**Conifers**	**Deciduous**	***H. pomanensis***	**Column Total (CT)**	**Producer Accuracy (%)**
Referencne data	Ground	56		3	1	60	93.3
	Conifers		27		5	32	84.4
	Deciduous	5	2	67	2	76	88.2
	H. pomanensis	4		5	42	51	82.4
	Row Total (RT)	65	29	75	50	219	
User accuracy (%)		86.2	93.1	89.3	84	**Overall accuracy (%)**	**87.7**

Table 17: Point based accuracy assessment of *Bhattacharya* classifier error matrix using combined reference data (N_3 =219) across all land cover type classes.

	Class	**Ground**	**Conifers**	**Deciduous**	***H. pomanensis***	**Column Total**	**Producer Accuracy (%)**
Reference data	Ground	56		2		58	96.6
	Conifers	1	35		2	38	92.1
	Deciduous	21		52		73	71.2
	H. pomanensis	4		1	45	50	90
	Row Total	82	35	55	47	219	
User accuracy (%)		68.3	100	94.5	95.7	**Overall accuracy (%)**	**85.8**

The error matrices of the best two performing classifiers were analysed so as to compute kappa statistics in order to conduct hypothesis testing so as to ascertain whether the *Maxver* classifier had a higher mapping accuracy than the *Bhattacharya* classifier. Results of the point based accuracy assessment using the combined reference data (N_3=219) showed that the *Maxver* classifier had user and producer accuracies greater than 82% across all land cover types (Table 16). The *Bhattacharya* classifier on the other hand had the highest producer accuracies (i.e. lowest omission errors) than the *Maxver* except for the deciduous trees land cover type (Table 17). Furthermore, the *Bhattacharya* classifier had user accuracies above 94% for all land cover type classes, except for the ground class, whereas the commission and omission errors of the *Maxver* classifier were similar across all land cover type classes (Table 6). Statistical hypothesis testing was conducted to determine whether the $\hat{k}$ values of the two best performing classifiers i.e. *Maxver* and *Bhattacharya* in Table 15 were significantly different, hereafter denoted as $\hat{k}_M$ and $\hat{k}_B$, respectively. The results in Table 18 show the statistics used to calculate the standard normal deviate Z_{MB} between $\hat{k}_M$ and $\hat{k}_B$. Z_{MB} was calculated to be equal to 0.4983 (i.e. less than 1.96) therefore the null hypothesis that the

Maxver classifier might not have given better classification results than the *Bhattacharya* classifier not rejected at the 95% confidence level.

Table 18: Statistics for the hypothesis test.

Classifier	p_oX	p_cX	$\hat{k}_X$	var_$\hat{k}_X$
Maxver	0.8767	0.2727	0.8305	0.000871784
Bhattacharya	0.8584	0.2596	0.8088	0.001020260

Where p_oX, p_cX and var_$\hat{k}_X$ represent the overall accuracy, chance agreement and the variance of Kappa, respectively for image classifier X.

Moreover, a comparison between the Bhattacharya and Maxver classifier areal estimates of *H. pomanensis* areal estimates was conducted to assess the omission errors associated with these techniques. Overall, the *Bhattacharya* classifier mapped very small *H. pomanensis* clumps with less omission error than the *Maxver* classifier with corresponding unmapped areal estimates of 9.3% and 37.8%, respectively (Table 19). While the pattern in mapping performance of the two classifiers across different area sizes of *Harrisia pomanensis* clumps is not clear, the results indicated that the *Bhattacharya* classifier gives the highest estimates of *H. pomanensis* for area sizes below 9 m^2 and between 12 and 21 m^2 compared to the *Maxver* classifier (Table 19). In addition, almost similar mapping performance by the *Bhattacharya* classifier was demonstrated for area sizes between 9 m^2 to 12 m^2 and 21 m^2 to 61 m^2 relative to the *Maxver* classifier (Table 19). These results suggest that the *Bhattacharya* classifier maps *H. pomanensis* with the lowest omissions below 22% meanwhile the reported *Maxver* omission errors were up to approximately 40%.

Table 19: Mapping or detection areal estimates for the *Maxver* and *Bhattacharya* classifiers.

			***Maxver* classifier**		***Bhattacharya* classifier**	
Number of polygons (n)	Polygon size (m^2)		Mapped area (%)	Unmapped area (%)	Mapped area (%)	Unmapped area (%)
10	Very small - Small	0 - 9	62.2	37.8	90.7	9.3
8	Small - Medium	9 -12	60.7	39.3	84	16
8	Medium - Large	12 - 21	74.3	25.7	91.1	8.9
9	Large – Verylarge	21 - 61	63.6	36.4	78.4	21.6

To demonstrate commission error occurrence for the *Maxver* and *Bhattacharya*, extracts of the RGB UAV orthomosaic depicting *H. pomanensis* clumps were digitized with a red polygon and subsequently the polygons were coloured blue and compared with each classifier's thematic map to show how each classifier mapped the plant clump. This was to illustrate how each classifier omitted *H. pomanensis* pixels and mapped them as another class (Figure 15 and 16). The *Maxver* classifier has more mixed classes within the digitized polygons that the *Bhattacharya* classifier, and these qualitative area based accuracy results show the same pattern as point based accuracy assessment results in Tables 14-17.

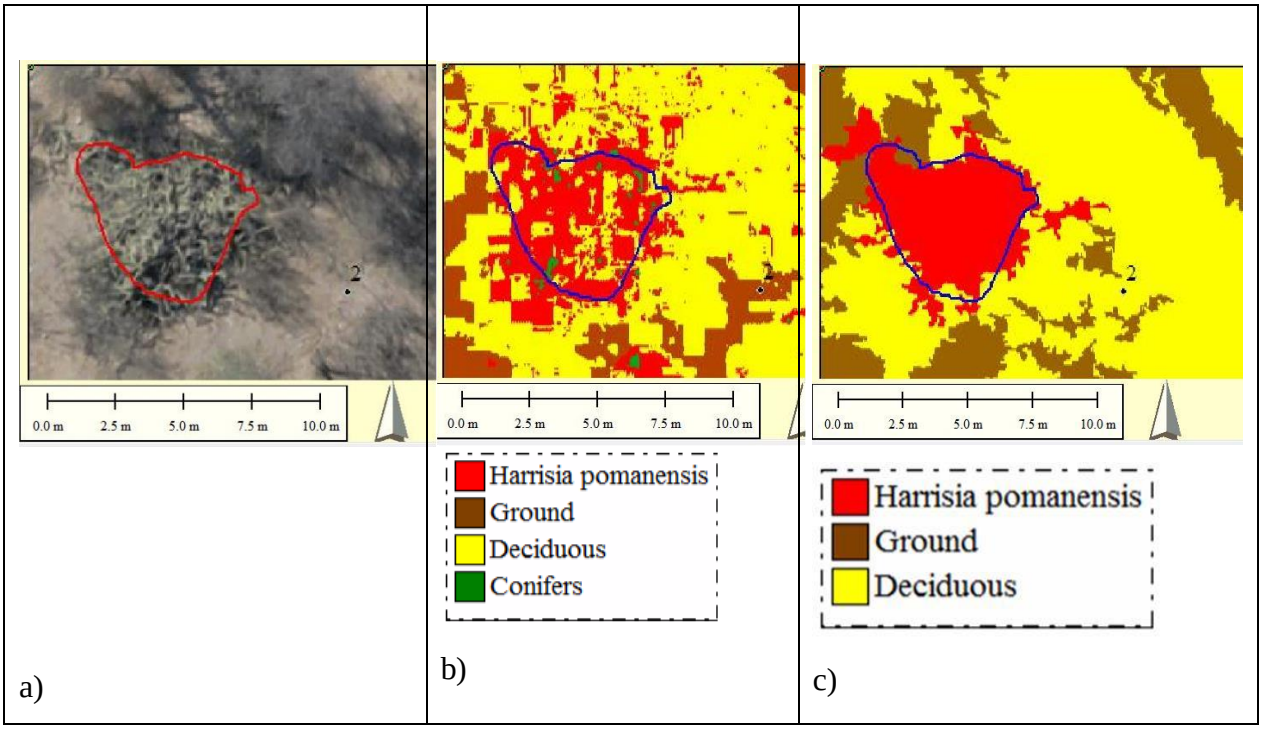

Figure 17: a) An extract of the UAV RGB image depicting a clump of *H. pomanensis* delineated by a visually interpreted 4.7 m2 reference polygon in red, b) Selection of the Maxver classification map results for the same reference polygon and c) Selection of the *Bhattacharya* classification for the same reference polygon. In this scene there is no *H. pomanensis* plants far below (South) the polygon but the *Maxver* classifier (Figure 15b) committed a tree into the *H. pomanensis* class (red theme below the polygon).

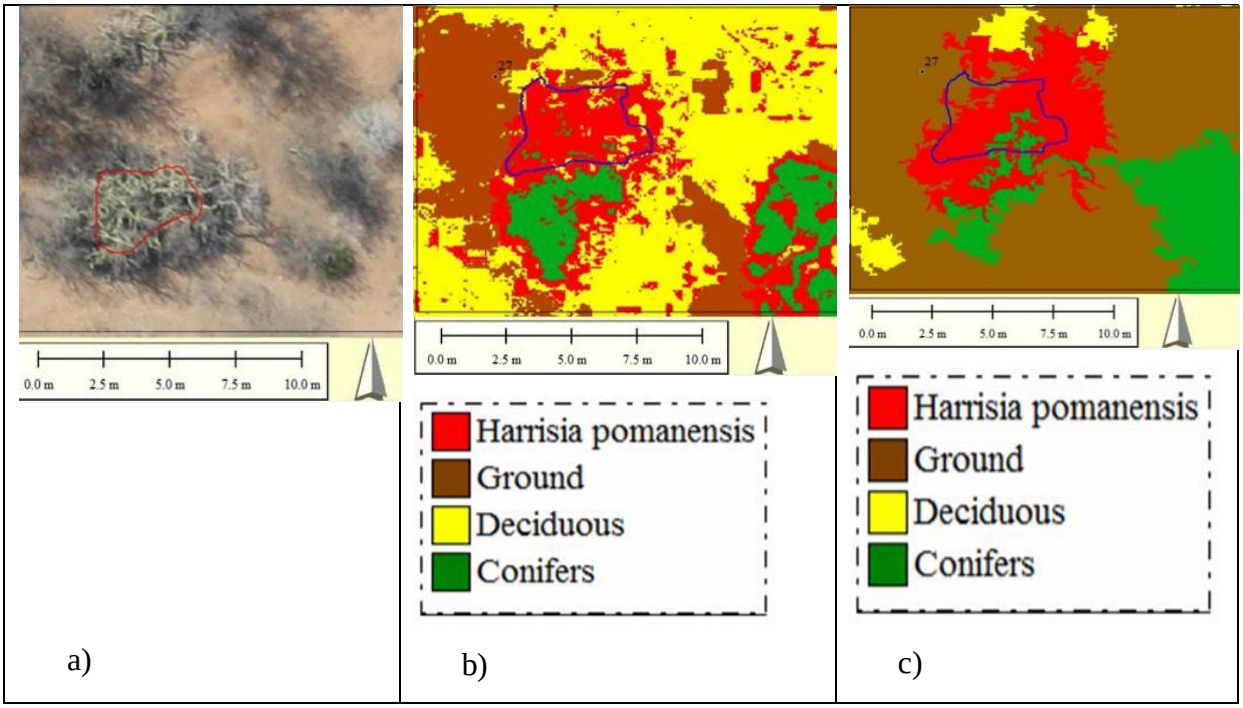

Figure 18: An extract of the 5 cm UAV RGB image depicting a clump of *H. pomanensis* delineated by a 22 m^2 visually interpreted reference polygon in red, b) Selection of the *Maxver* classification map results for the same reference polygon and c) Selection of the *Bhattacharya* classification for the same reference polygon. In this scene, there is not a significant amount of the *H. pomanensis* plant spikes outside the polygon and therefore both *Maxver* classifier and Bhattacharya classifier committed other attributes into the *H. pomanensis* class. It seems that the Bhattacharya classifier committed more than the *Maxver* classifier in this scene immediately around the polygon. However, the *Bhattacharya* classifier detected the conifer (green theme) on the right bottom corner better than the *Maxver* classifier.

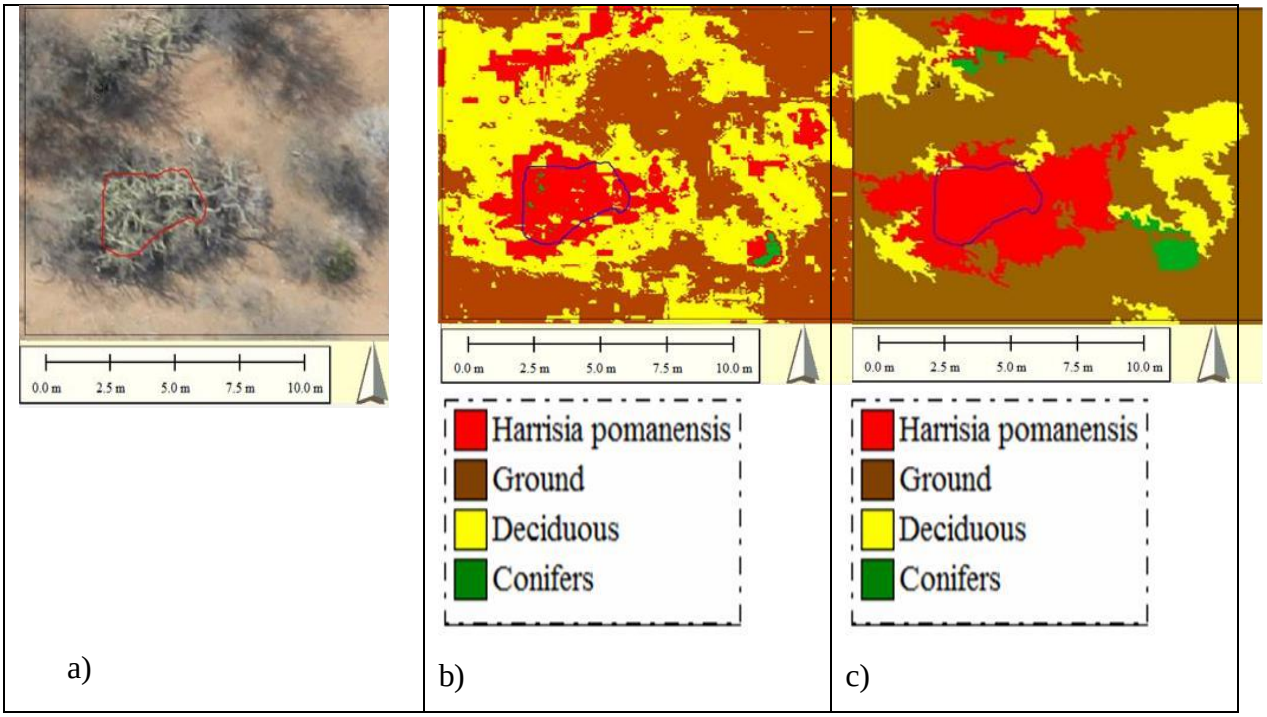

Figure 19: An extract of the 5 cm UAV RGB image depicting a clump of *H. pomanensis* delineated by a visually interpreted reference polygon in red, b) Selection of the *Maxver* classification map results for the same reference polygon and c) Selection of the *Bhattacharya* classification for the same reference polygon. On the far North side in this scene there is a clump of *H. pomanensis*. Both classifiers detected that clump but it seems that both of them overestimated its extent.

4.4. Comparison of the uncalibrated and the calibrated orthomosaics for the *Bhattacharya* classifier.

The assessment of whether radiometric calibration improves mapping accuracy was performed using the *Bhattacharya* classifier. Results on Tables 20 and 21, show that based on the 21 randomly generated reference points, the *Bhattacharya* classifier produced overall accuracies of 66.7% ($\hat{k} = 53.5$) and 76.2 % ($\hat{k} = 64.5$), respectively. The 9.5% difference could be sufficient to infer that radiometric calibration does increase mapping accuracy but final inference will be made when the entire orthomosaic is considered instead of only considering the centre tile B2 with only 21 reference points.

Table 20: Point based accuracy assessment of *Bhattacharya* classifier error matrix using reference data (N_5 =21) for the uncalibrated centre tile B2.

	Class	**Ground**	**Conifers**	**Deciduous**	***H. pomanensis***	**Column Total**	**Producer Accuracy (%)**
Reference data	Ground	3		1	1	5	60.0
	Conifers	1	1	1		3	33.3
	Deciduous			4		4	100
	H. pomanensis	3			6	9	66.7
	Row Total	7	1	6	7	21	
User accuracy (%)		42.9	100	66.7	85.7	**Overall accuracy (%)**	**66.7**

Table 21: **.** Point based accuracy assessment of Bhattacharya classifier error matrix using reference data (N_5 =21) for the calibrated centre tile B2.

	Class	**Ground**	**Conifers**	**Deciduous**	***H. pomanensis***	**Column Total**	**Producer Accuracy (%)**
Reference data	Ground	6				6	100
	Conifers						
	Deciduous			4	1	5	80.0
	H. pomanensis	1	1	2	6	10	60.0
	Row Total	7	1	6	7	21	
User accuracy (%)		85.7	0.0	66.7	85.7	**Overall accuracy (%)**	**76.2**

CHAPTER 5

5. Discussion and Conclusions

5.1. Chapter outline

This study presents a framework for semi-automated object-based image classification of IAPs in South Africa using *H. pomanensis* as a case study. The proposed UAV-RS framework made use of four general methods namely (1) geometric calibration of a consumer grade camera, (2) radiometric calibration of a UAV-derived orthomosaic, (3) evaluation of five image classification techniques and (4) determination of whether radiometric calibration improves image classification accuracy.

5.2. Geometric camera calibration

The geometric calibration results of the Sony Nex-7 camera showed less tangential distortions than radial distortions and this can be attributed to the short range from which the LCD screen images were taken. However, the main aim of conducting geometric calibration was to import this information into the SfM mosaicking software (i.e. Agisoft Photoscan) so that the software can be aware of the camera intrinsic parameters. Other ancillary datasets that were imported into Agisoft Photoscan were the camera exterior orientation parameters (i.e. the roll, pitch and yaw of the UAV as recorded by the on-board IMU), the geographic positions from which each photo was taken as recorded by the on-board GNSS and the field surveyed GCPs. The GNSS/IMU data helped increase image mosaicking speed while the GCPs helped produce an accurately georeferenced orthomosaic.

5.3. Vicarious radiometric calibration

On the other hand, the vicarious radiometric calibration approach made use of the empirical line method (ELM) for large scale mapping applications as IAPs tend to spread over large spatial extent areas. This approach included (1) calibration target design whereby large enough and highly Lambertian calibration targets were created, (2) a scene illumination uniformity check experiment as solar illumination changes rapidly through short time and space, (3) the vicarious ELM to regress image DNs against *in situ* measured mean reflectance values, and (4) the radiometric calibration accuracy assessment using the PVC check targets.

Firstly, calibration target design results demonstrated that the relatively affordable Masonite hardboards painted with varying grey values of black and white water paint are highly Lambertian and appropriate for use in calibration target design. This property was observed both in a controlled room with an artificial light source and on the field in the semi-arid woodland study area. The Masonite hardboards of 244cm x 122cm were found to be large enough to allow painting of 2 grey levels in tandem configuration when the UAV is flown at an altitude of less than 160m AGL. Some studies make use of vinyl sheet canvas to design the greyscale calibration targets as done in Del Pozo et al. (2014) and thus, the target material of choice can be influenced not only by Lambertian properties but also availability, transportability and ease of use in different environmental settings.

Secondly, a scene illumination uniformity check method was developed in this study to assess whether the incoming radiant flux is uniform across the orthomosaic. The solar irradiance within the 97ha study area was found to be uniform thus indicating that all the 611 images taken by the Sony NEX-7 on-board the UAV were acquired under the same environmental conditions. The hypothesis was that under the same environmental conditions, the digital numbers of the same target material should be similar and this was tested at a 95% confidence interval. The difference of 1.36 between the mean DNs of the reference L-target and the other L-targets in Table 9 was found not to be statistically significant at the 95% confidence interval and from this, it was inferred that it is justifiable to calibrate the entire scene using prediction equations derived using mean reflectance values measured from only a single spot within the mapped area.

Thirdly, this study demonstrated that there exists an exponential relationship between target DNs and their corresponding at-surface mean reflectance values (equations 11-13) in Table 10. However, in most studies, for example in Dean et al., (2000), Karpouzli and Malthus (2003) Levin et al., (2009) and Berni et al., (2009), the empirical linear calibration equation were derived by assuming a linear relationship between image DNs and calibration targets *in situ* reflectance values. This assumption is usually made when there is only two calibration targets e.g. a white and a black target (Smith and Milton, 1999). In this study, this relationship was found to be exponential with coefficient of determination R^2 values greater than 0.98 (equations 11-13, Table 10) as found in Wang and Myint (2015). Figure 12 is an example of the observed exponential relationship between image DNs and the mean *in situ* measured reflectance values of the calibration targets. Upon transformation of the exponential equations by taking the natural log, the constant calibration parameters of the empirical linear

equations were derived. The three ELM calibration prediction equations were then derived by first computing the gradient of the prediction equation using the calibration target average DN and its average *in situ* reflectance as well as the constant calibration parameter or y-intercepts of the linear equations (Table 18).

Finally, the accuracy of at-surface reflectance values in the calibrated image wavebands was assessed using *in situ* spectral measurements for white, red, green, blue and black reinforced PVC targets resulting in a correlation coefficient r 0.96 (p<0.01) and overall RMSE of 0.063. These findings suggest that given the entire scene being mapped is experiencing similar irradiance flux under similar environmental conditions according to the scene illumination uniformity assessment, then radiometric calibration using mean reflectance values measured from only one area of the orthomosaic can be used to calibrate the entire orthomosaic. The proposed framework is not only important for mapping IAPs but also for use in large scale crop mapping applications in precision agriculture, land use/ land cover monitoring as well as vegetation mapping and classification, particularly for mapping widespread invasive alien plants such as *H. pomanensis*.

The limitation of this research is that it has no way of showing the largest spatial coverage for which the demonstrated vicarious radiometric calibration framework could be applied. This however, could also depend on the nature of the environment that is being mapped as well as prevailing weather conditions. Future research objectives could be to apply this framework for areas larger than 200ha as the developments in UAV and battery technology are increasingly enabling these systems to map larger areas. Most studies that applied UAV-RS for mapping IAPs made use of thematic image classification without conducting either sensor geometric or image radiometric calibration, for instance Dvořák et al., 2015, Müllerová et al., 2016, Müllerová et al., 2017, Hill et al., 2017 and Mafanya et al., 2017. Therefore, another future research objective would be to assess if radiometric calibration improves the image classification accuracy for mapping and detecting various IAPs in different environmental settings. Another important research avenue is quantitative image analysis using radiometric calibrated UAV-RS imagery for improving the estimation of biophysical and biochemical constituents in plants from UAV imagery.

5.4. The influence of radiometric calibration on mapping accuracy.

The null hypothesis that the *Maxver* classifier might not have given better classification results than the *Bhattacharya* classifier could not be rejected at the 95% confidence level. In addition, for the point based accuracy assessment based on the combined reference points (N_3 =219), the *Maxver* and *Bhattacharya* classifiers had 17.6% and 10% omission errors for the *H. pomanensis* class, respectively. Moreover, for the area based accuracy assessment, the *Maxver* and *Bhattacharya* classifiers had overall omission errors of 34.8% and 13.95%, respectively for mapping *H. pomanensis*. As a result, it was inferred that the *Bhattacharya* classifier maps *H. pomanensis* better than the *Maxver* classifier. Thus the assessment of whether radiometric calibration improves mapping accuracy was performed using the *Bhattacharya* classifier. Results on Tables 20 and 21, show that based on 21 randomly generated reference points, the *Bhattacharya* classifier produced overall accuracies of 66.7% ($\hat{k}$ = 53.5) and 76.2 % ($\hat{k}$ = 64.5) for the non-calibrated and the calibrated B2 tile, respectively. The 9.5% difference could be sufficient to infer that radiometric calibration does increase mapping accuracy. However, the influence of radiometric calibration on mapping accuracy can further be ascertained when entire orthomosaic is considered instead of only considering the centre tile B2 with only 21 reference points.

5.5. Evaluation of image classifiers

The image classification accuracy assessment made use of two interlinked evaluation strategies (i.e. point and area based accuracy assessment). The point based accuracy assessment results illustrated that the supervised image classifiers evaluated in this study generally produced better user, producer and overall accuracies than the unsupervised classifiers for mapping *H. pomanensis*. The poor performance of the unsupervised image classifiers could be attributed to the low spectral resolution (approximately 100nm wide bands) of the utilized UAV imagery (Müllerová et al., 2016). The evaluated unsupervised image classifiers depend only on the spectral information of the imagery because they make use of a comparison to assign a pixel/segment to a class according to a similarity measure that only takes into account a spectral mean or a median vector of the pixel/segment (Wang et al., 2005). It is thus expected that for low spectral resolution UAV imagery, too many pixels/segments that belong to different land cover types will have similar spectral vectors

and thus be classified together when they actually belong to different classes. This is explained by the generally low user and producer accuracies for the *K-mediuns*, *Euclidian length* and *Isoseg classifiers*.

On the other hand, the supervised classifiers make use of probability models to assign pixels/segments to a class and as a result, this could be one of the underlying reasons why these classifiers outperformed the unsupervised classifiers for mapping *H. pomanensis* from low spectral resolution UAV-derived imagery (Müllerová et al., 2016; Wang and Zhang, 2014). In addition to the probabilistic models, supervised image classifiers make use of training data-sets to guide the classifier using not only single pixels/segments but a sample group of pixels/segments to train the classifier through machine learning (Senseman et al., 1995).Consequently, the use of error matrices based on the combined reference points (N_3 = 219) to compare the classifiers that were selected as the best performing classifiers (i.e. the supervised *Maxver* and *Bhattacharya* classifiers) was made in section 4.2. On average, the object based *Bhattacharya* classifier gave higher producer and user accuracies than the pixel based *Maxver* classifier. However, the *Maxver* classifier gave a higher overall accuracy (87.7%) than the Bhattacharya classifier (85.8%) for the combined set of reference points (N_3 = 219). In addition to this, the *Maxver* classifier produced a higher Kappa statistic estimate ($\hat{k}_M$ = 0,8305) than the *Bhattacharya* classifier ($\hat{k}_B$ = 0,8088) but the difference between these two kappa values was shown not be to be statistically significant at the 95% confidence interval in section 4.3.

To determine which classifier was the most accurate for mapping *H.pomanensis*, area based accuracy assessment was conducted. In particular, the area based accuracy assessment showed that the *Bhattacharya* classifier mapped *H. pomanensis* better than the *Maxver* classifier with mapping accuracy averages of 86.1% and 65.2% for all the different polygon sizes, respectively. Additionally, the *Maxver* classifier produced thematic maps with the infamous salt and pepper effect. From these results we can deduce that the *H. pomanensis* spatial extent of 5.9ha/87.2ha that was estimated by the *Bhattacharya* classifier with 90% and 95.7% producer and user accuracy, respectively, is more accurate. With reference to the combined reference points (N_3 = 219) and the area based accuracy assessment, it is inferred that the *Bhattacharya* classifier produced the most accurate classification and spatial extents estimates for mapping *H. pomanensis* than any other classifier in the Table 15 evaluation. This most accurate *H. pomanensis* mapping by the *Bhattacharya* classifier is demonstrated in

Figures 15 and 16. The *Bhattacharya* classifier is therefore recommended for mapping *H. pomanensis* in semi-arid rangelands. These findings are in agreement with other studies in that object based image classification methods are more accurate for classifying for very high spatial resolution (<5cm) but low spectral resolution (~100nm) imagery than pixel based classification techniques (Laliberte et al., 2011; MacLean and Congalton, 2011; Lary et al., 2016). For instance, Laliberte (2011) obtained 86% overall accuracy ($\hat{k} = 0.81$) for vegetation mapping in an arid rangeland plot using a supervised object based classification approach. The increased OBIA classification accuracy can partly be attributed to image segmentation algorithms such as the region growing technique which creates objects that have a spatial or spectral homogeneity in one or more dimensions (Blaschke, 2010).

Moreover, it is possible to incorporate OBIA into the automation or semi-automation of remote sensing image classifiers (Benz et al., 2004). It should be noted that although image segmentation and classification algorithms can be improved for various applications, other factors such as environmental conditions during the data acquisition need to be considered. For instance in this study, *H. pomanensis* was mapped in late winter (13 August 2015 and 12 August 2016) when the species was in a phenological stage that makes it different from the background woodland vegetation and when the deciduous trees were leafless. The timing of the survey contributed to the success of OBIA. Moreover, OBIA was successful in mapping *H. pomanensis* as it takes into consideration spatial and textural information as *H. pomanensis* has both a different shape and texture compared to the other plants in the study area. The UAV remote sensing sub-field is a promising approach for future mapping and detection of IAPs. This is because UAV remote sensing allows for mapping in inaccessible areas like the thorny woodland considered in this case study.

Another advantage is that IAPs management practitioners in the future will likely have access to affordable integrated UAV and sensor systems than they do with traditional aircraft systems or satellite data (Dvořák et al., 2015). Moreover, the high spatial resolution which can be attributed to the associated low UAV flight heights allows IAPs management practitioners to visually locate IAPs communities and clusters from true colour orthomosaics even before image classification. Advancements in battery technology, miniaturization of multispectral and hyperspectral sensors and design of more compact UAV and sensor systems all form a basis upon which better management, monitoring and eradication of IAPs will be possible in the future as spatial data is important for these IAPs management goals.The limitation of this study is that *H. pomanensis* is sometimes found as an understory

occurring invasive alien plant species. Thus all estimates based on aerial imagery might under estimate the true extent of *H. pomanensis* by not accounting for the clumps or stems that might be hiding underneath deciduous and coniferous trees. The problem of understory occurring invasive alien plant species has been frequently identified in remote sensing research (Fox et al., 2009; Peerbhay et al., 2016; Huang and Asner, 2009).

Remote Sensing methods for improving detection of understorey invasive alien plant species have been presented by Joshi et al. (2006), Wang et al. (2009) and Tuanmu et al. (2010). An inherent limitation in the use of UAVs is the relatively small spatial extent when compared to airborne and satellite platforms. Additionally, low flight altitudes mean more images which may be labour intensive or require too much computing power for processing. When compared to traditional aerial surveying orthomosaics, UAV imagery orthorectification or georeferencing requires more GCPs and the surveying of GCPs is labour intensive. The point-based accuracy assessment results showed that with reference to the combined set of reference points (N_3 = 219), the supervised image classifiers mapped *H. pomanensis* better than the unsupervised classifiers with user and producer accuracies of 82.4% and 84% for the *Maxver* classifier as well as 90% and 95.7% for the *Bhattacharya* classifier. Even though the object based *Bhattacharya* classifier gave higher user and producer accuracies than the pixel based *Maxver* classifier, the *Maxver* gave the highest overall accuracy of 87.7% and the highest $\hat{k}$ of 0.8305. A statistical hypothesis test was then conducted to test whether the *Maxver* $\hat{k}$ of 0.8305 was significantly greater than the Bhattacharya Kappa estimate of 0.8088 and we could not reject the null hypothesis that the two values are not statistically different at the 95% confidence interval. Additionally, the area based accuracy assessment results show that the *Bhattacharya* and *Maxver* classifiers estimated the spatial extent of *H. pomanensis* with an average detection accuracy of 86.1% and 65.2%, respectively.

The area based accuracy assessment results also show that the *Bhattacharya* classifier was able to accurately map both small and large clumps of *H. pomanensis*. The Bhattacharya classifier is therefore recommended for mapping *H. pomanensis* under the current or similar environmental settings. These findings would be used to support the development of a semi-automated image classification system for mapping and monitoring *H. pomanensis*. The generic workflows in this scheme could be used for mapping other IAPs.

6. REFERENCES

Agisoft LLC. Agisoft PhotoScan. Available online: http://www.agisoft.com/downloads/installer/

Agjee, N.; Mutanga, O.; Ismail, R.Remote sensing bio-control damage on aquatic invasive alien plant species. *South African Journal of Geomatics*. **2015**, 4(4), 464-485.

Akar, Ö. Mapping land use with using Rotation Forest algorithm from UAV images. *International Journal of Remote Sensing.***2017**, 50(1): 269-279.

Babapour, H.;Mokhtarzade, M.; Valadan Zoej, M.J. A novel post-calibration method for digital cameras using image linear features. *International Journal of Remote Sensing*.**2017**, 38(8-10):2698-2716.

Bagheri, N. Development of a high-resolution aerial remote sensing system for precision agriculture. *International Journal of Remote Sensing.***2017**, 38(8-10):2053-2065.

Balletti, C; Guerra, F; Tsioukas, V; Vernier, P. Calibration of Action Cameras for Photogrammetric Purposes. *Sensors*. 2014; 14(9):17471-17490

Bareth, G.; Aasen, H.; Bendig, J.; Köln; Gnyp, M. L.; Dülmen; Bolten, A.; Köln, Jung, A.; Leipzig, M. R.Ulm, Oulu, J. S. Low-weight and UAV-based Hyperspectral Full-frame Cameras for Monitoring Crops: Spectral Comparison with Portable Spectroradiometer Measurements. Schweizerbart'sche Verlagsbuchhandlung, Stuttgart, Germany. 2015:1-11.

Bendig, J.; Bolten, A.; Bareth, G. Introducing a low-cost mini-UAV for thermal and multispectral imaging. *The International Archives of the Photogrammetry, Remote Sensing and Spatial Information Sciences.* 2012,XXXIX-B1, Melbourne, Australia.

Benz, C.; Hofmann, P.; Willhauck, G.; Lingenfelder, I.; Heynen, M. Multiresolution, object-oriented fuzzy analysis of remote sensing data for GIS-ready information. *ISPRS Journal of Photogrammetry and Remote Sensing*. **2004**, 58: 239-258

Blaschke, T.; Strobl, J. What's wrong with pixels? Some recent developments interfacing remote sensing and GIS. Geo-Informations-Systeme. **2001**, 14(6), 12-17.

Blaschke, T. Object based image analysis for remote sensing. *ISPRS Journal of Photogrammetry and Remote Sensing*. **2010**,65:2-16.

Bonnet, S.; Lisein, J; Lejeune, P. Comparison of UAS photogrammetric products for tree detection and characterization of coniferous stands. *International Journal of Remote Sensing.* **2017**, 38(19), 5310-5337.

Calvino-Cancela, M, Me´ndez-Rial R, Reguera-Salgado J, Martın-Herrero J.Alien Plant Monitoring with Ultralight Airborne Imaging Spectroscopy. *PLoS ONE* .**2014**, 9(7): e102381. doi:10.1371/journal.pone.0102381.

Camara, G.; Souza R. C. M.; Freitas, U. M.; Garrido, J.; SPRING: Integrating remote sensing and GIS by object-oriented data modelling. *Computers & Graphics*, **1996**, 20(3), 395-403.

Candiago, S.; Remondino, F.;,De Giglio, M.;Dubbini, M.; Gattelli, M. Evaluating Multispectral Images and Vegetation Indices for Precision Farming Applications from UAV Images. *Remote Sens*. **2015**, 7(4): 4026-4047.

Chance, M. C;Coops, N. C.; Plowright, A. A. Tooke, T. R.; Christen A, Aven, N. Invasive shrub mapping in an urban environment from hyperspectral and lidar-derived attributes. Frontiers in plant science. 2016,7, 1528.

Chandler G. And Merry C. South African Geoid 2010: SAGEOID10. *Surveying Technical: PositionIT*. **2010**,29-33.

Chen, G.; Zhao, K.; Powers, R. Assessment of the image misregistration effects on object-based change detection. *ISPRS Journal of Photogrammetry and Remote Sensing*. **2014**,87:19-27

Choi, E.; Lee, C. Feature extraction based on the Bhattacharyya distance. *Pattern Recognition* **2003**, 36, 1703-1709

Clout, M.N. & Williams, P.A. Invasive species management. A handbook of principles and techniques. Oxford University Press, Oxford, **2009**.

Congalton, R. G. A review of assessing the accuracy of classifications of remotely sensed data. Remote Sens. Environ **1991**, 37, 35-46.

Congalton R. G.; Oderwald, R. G.; Mead R. A. Assessing Landsat classification using discrete multivariate statistical techniques. *Photogramm. Eng. Remote Sens*. **1983**, 46(12), 1671-1678.

Coveney, S.; Roberts, K. Lightweight UAV digital elevation models and orthoimagery for environmental applications: data accuracy evaluation and potential for river flood risk modelling. International Journal of Remote Sensing.**2017**,38(8-10):3159-3180.

Cracknell, A. P. UAVs: regulations and law enforcement. *International Journal of Remote Sensing*. **2017**, 38(8-10), 3054-3067.

Crusiol, L. G. T.;Nanni, M. R.; Silva, G. F. C.; Furlanetto, R. H.; Gualberto, A. A. Gasparotto, A. C.; De Paula, M. N. Semi-professional digital camera calibration techniques for Vis/NIR spectral data acquisition from an unmanned aerial vehicle. *International Journal of Remote Sensing*. **2017**, 38(8-10), 2717-2736.

Dehaan, R.L.; Weston, L. A.; Rumbachs, R. The design and the development of a hyperspectral unmanned aircraft mapping system for the detection of invasive plants. Eighteenth Australian Weeds Conference. **2012**: 103-107.

Del Pozo, S.; Rodríguez-Gonzálvez, P.; Hernández-López, D.; Felipe-García, B. Vicarious Radiometric Calibration of a Multispectral Camera on Board an Unmanned Aerial System. *Remote Sens*. **2014**, 6: 1918-1937. doi:10.3390/rs6031918.

De Maesschalck, R.; Jouan-Rimbaud, D.; Massart, D. L. The Mahalanobis distance. *Chemometrics and Intelligent Laboratory Systems***. 2000**, 50, 1-18.

DiPietro, D. Mapping the invasive plant *Arundo donax* and associated riparian vegetation using hyperspectral remote sensing. MS Thesis in Geography, University of California Davis.**2002**.

DiPietro, D., Ustin, S.L., Underwood, E.Mapping the invasive plant Arundo donax and associated riparian vegetation using AVIRIS. Proceedings of the 11th Earth Science Airborne,Workshop, Jet Propulsion Laboratory, Pasadena, CA, March 6-8, **2002**.

Dlamini, W. M. Multispectral detection of invasive alien plants from very high resolution 8-band satellite imagery using probabilistic graphical models. **2010**, 1-17.

Duda, R. O.; Hart P. E. Pattern Classification and Scene Analysis. John Wiley and Sons, New York, USA,**1973**

Dvořák, P.; Müllerová, J.; Bartaloš, T.; Brůna, J. Unmanned aerial vehicles for alien plant species detection and monitoring. *The International Archives of the Photogrammetry, Remote Sensing and Spatial Information Sciences*. **2015**, XL-1/W4, 83-90.

Evangelista, P.H.; Stohlgren, T.J.; Morisette, J.T.; Kumar, S.Mapping invasive Tamarisk (Tamarix)—A comparison of single-scene and timeseries analyses of remotely sensed data. *Remote Sens.* **2009**, 1(3), 519–533.

Femondimo, F.; Barazzetti, L.; Nex, F.; Scaioni, M.; Sarazzi, D. UAV Photogrammetry for mapping and 3D modelling- current status and future perspectives. *The International Archives of the Photogrammetry, Remote Sensing and Spatial Information Sciences*. **2011**, XXXVIII-1/C22, 25-30.

Fernández-Hernandez González-Aguiler, D.; Rodriguez-Gonzalvez, P.; Mancera-Taboada, J. Image-based modelling from unmanned aerial vehicle (UAV) photogrammetry: An effective low-cost tool for archeological applications. *Archeometry*.**2015**, 57(1), 128-145.

Filho, R. A., Vitorello I. and Bins L. S. A (1997). Application of image merging, segmentation and region-classification techniques as a new approach for the detailed thematic mapping of soil-vegetation assemblages. *Revista Brasileira de Geociências* **1997**, 27(2), 203-206.

Fox, J. C.; Buckley, Y. M.; Panetta, F. D.; Bourgoin, J.; Pullar, D. Surveillance protocols for management of invasive plants: modeling Chilean needle grass (*Nassella neesiana*) in Australia. *Diversity Distrib*. **2009**, 12,577-589.

Fraser, R. H.; Olthof, I.; Lantz, T. C.; Schmitt, C. UAV photogrammetry for mapping vegetation in low-artic. *Arctic science.***2016**, 2:79-102.

Gini, R.; Pagliari, D.; Passoni, D.; Pinto L.; Sona, G.; Dosso, P. UAV photogrammetry: Block Triangulation Comparisons. *ISPRS - Archives*, **2013**, XL-1/W2, 157-162.

Guanter, L., Segl, K., & Kaufmann, H. Simulation of optical remote-sensing scenes with application to the EnMAP hyperspectral mission. *IEEE Transactions on Geoscience and Remote Sensing*, **2009**, 47(7), 2340-2351.

Gómez-Candón, D.; De Castro, A. I.; Lopez-Granados, F. Assessing the accuracy of mosaics from unmanned aerial vehicle (UAV) imagery for precision agriculture purposes in wheat. *Precision Agric.* **2014**, 15, 44-56.

Hakala, T.; Suomalainen, J.; Peltoniemi, J.I Acquisition of Bidirectional Relectance Factor Dataset Using a Micro Unmanned Aerial Vehicle and a Consumer Camera. *Remote Sens.***2010**, 2(3): 819–832.

Hantson, W.; Kooistra, L.; Slim, P. A. Mapping invasive woody species in coastal dunes in the Netherlands: a remote sensing approach using LiDAR and high-resolution aerial photographs. Applied Vegetation Science. **2012**, 15: 536-547.

Hedling, G.; Parker, A.; Wonnacott, R.TrigNet The Network of Active GPS Base Stations for South Africa. *Proceedings of the 13th International Technical Meeting of the Satellite Division of The Institute of Navigation (ION GPS 2000)*, **2000**, 1865-1870.

Hellesen, T.; Matikainen, L. An Object-Based Approach for Mapping Shrub and Tree Cover on Grassland Habitats by Use of LiDAR and CIR Orthoimages. *Remote Sens.* **2013**, 5(2): 558-583.

Hill, D. J.; Tarasoff, C.; Whitworth, G. E.; Baron, J.; Bradshaw, J. L; Church, J.S. Utility of unmanned aerial vehicles for mapping invasive plant species: a case study on yellow flag iris (*Iris pseudacorus L.*). *International Journal of Remote Sensing.* **2017,** 38(8-12), 2083-2105.

Honkavaara, E.; Arbiol, R.; Markelin, L.;Martinez, L.; Cramer, M.;Bovet, S.; Chandelier, L.; Ilves, R.; Klonus, S.; Marshal, P.; Schläpfer, D.;Tabor, M.; Thom, C.;Veje, N. Digital Airborne Photogrammetry—A New Tool for Quantitative Remote Sensing?—A State-of-the-Art Review On Radiometric Aspects of Digital Photogrammetric Images. Remote Sensing. **2017**, 1, 577-605.

Honkavaara, E.; Saari, H.; Kaivosoja, J.; Pölönen, I.; Hakala, T.; Litkey, P.; Mäkynen, J.; Pesonen, L. Processing and Assessment of Spectrometric, Stereoscopic Imagery Collected Using a Lightweight UAV Spectral Camera for Precision Agriculture. Remote Sens. **2013**, 5: 5006-5039.

Huang, C.; Asner, G. P. Applications of remote sensing to alien invasive plant studies. *Sensors.***2009,** 9, 4869-4889.

Jay, S.; Lawrence, R.; Repasky, K.; Keith, C. Invasive species mapping using low cost hyperspectral imagery. **2009** ASPRS Annual Conference, Baltimore, Maryland.

Joshi, C.; De Leeuw, J.; van Andel, J.; Skidmore, A. K.; Lekhak, H. D.; van Duren, I.C; Norbu, N. Indirect remote sensing of a cryptic forest understorey invasive species. Forest ecology and management. **2006**, 225(1-3), 245-256.

Kandeh J. M. K., dos Santos J. L. C and Kumar L. Mapping invasive alien plants in South Africa. International Institute Geo-Information science and Earth Observation.**2001**:1-2.

Karpouzli, E.; Malthus, T.; The empirical line method for the atmospheric correction of IKONOS imagery. Int J. Remote Sensing, **2003**, 24(5):1143-1150.

Kelcey, J.; Lucieer, A. Sensor correction and radiometric calibration of a 6-band multispectral imaging sensor for UAV remote sensing. **2012**, *International Archives of the Photogrammetry, Remote Sensing and Spatial Information Sciences*, Volume XXXIX-B1, 393-398.

Laliberte, A. S. Image processing and classification procedures for analysis of sub-decimeter imagery acquired with an Unmanned Aircraft over arid rangelands. *GIScience and Remote Sensing*. **2011**, 48(1), 4-23.

Laurin, G. V.; Chan, J.C.; Chen, Q.; Lindsell, J A., Coomes, D, A. Guerriero, L.; Frate, F. Miglietta, F.; Valenti R. Biodiversity Mapping in a Tropical West African Forest with Airborne Hyperspectral Data. PLOS ONE, **2014**, 9(6) :1-10.

Lary, D.J.; Alavi A. H.; Gandomi, A. H.; Walker A. L. Machine learning in geosciences and remote sensing. Geoscience Frontiers, **2016**, 7, 3-10.

Le Maitre D.C., Forsyth G.G., Dzikiti S and Gush M.B. (2013). Estimates of the impacts of invasive alien plants on water flows in South Africa. *Water SA*. **2016**, 42(4), 659-672.

Lentilucci, E.J. On using and computing the Kappa statistic, Tech. Rep. Rochester Institute of Technology, College of Science, Center for Imaging Science, Digital Imaging and Remote Sensing Laboratory, Rochester, New York, United States, **2006**.

Li, W.; Niu, Z.; Chen, H.; Li, D. Characterizing canopy structural complexity for the estimation of maize LAI based on ALS data and UAV stereo images. *International Journal of Remote Sensing.***2017**, 38(8-10), 2106-2116.

Liu, Y.; Bian, L.; Meng, Y.; Wang, H.; Zhang, S.; Yang, Y. Shao, X.; Wang,B Discrepancy measures for selecting optimal combination of parameter values in object-based image analysis. ISPRS Journal of Photogrammetry and Remote Sensing. **2012**, 68: 144-156.

Liu, Y.; Wang, T.; Ma, L.; Wang, N. Spectral Calibration of Hyperspectral Data Observed From a Hyperspectrometer Loaded on an Unmanned Aerial Vehicle Platform. IEE Journal of selected topics in applied earth observations and remote sensing. 2014, 7(6): 2630- 2638.

Lucieer, A.; Robinson, S.; Turner, D.;Harwin, S.;Kelcey, J. Using a micro-UAV for ultra-high resolution multi-sensor observations of Antarctic moss beds. *Int. Arch. Photogramm. Remote Sens.* **2012,** XXXIX-B1, 429–433.

MacLean, M. G.; Congalton, R. G. Investigating issues in map accuracy when using an object-based approach to map benthic habitats. GIScience and Remote Sensing, **2011**, 48(4), 457-477.

Mafanya, M.; Tsele, P.; Botai, J.; Manyama, P.; Swart, B.; Monate, T. Evaluating pixel and object based image classification techniques for mapping plant invasions from UAV derived aerial imagery: *Harrisia pomanensis* as a case study. *ISPRS Journal of Photogrammetry and Remote Sensing*.**2017**, 129:1-11.

Marshall, V.; Lewis, M.; Ostendorf, B. Do additional bands (Coastal, NIR-2, Red-Edge and Yellow) in worldview-2 Multispectral imagery improve discrimination of invasive tussock, Buffel Grass (Cenchrus Ciliaris)?. *International Archives of the Photogrammetry, Remote Sensing and Spatial Information Sciences*. **2012**, XXXIX-B2, Melbourne, Australia.

Miguel, E. Fernández-Renau, A, Prado, E; Jimenez, M. The processing of CASI-1500i data at INTA PAF. EARSel eProceeedings **2014,** 13,1.

Mitchell, J., Glenn, N., Sankey, T., Derryberry, D., Anderson, M., & Hruska, R. Spectroscopic detection of Nitrogen concentrations in sagebrush: implications for hyperspectral remote sensing, *Remote Sensing Letters*.**2012**, 3, 285-294.

Müller R. J. Avbelj E. Carmona, A. Eckardt , B. Gerasch , L. Graham , B. Günther , U. Heiden , J. Ickes , G. Kerr , U. The new hyperspectral sensor DESIS on the multi-payload platform muses installed on the ISS. *The International Archives of the Photogrammetry, Remote Sensing and Spatial Information Sciences*,XLI-B1, 12-19 July 2016, Prague, Czech Republic.

Knodt e, D. Krutz d, H. Krawczyk a, A. Makarau a, R. Miller b, R. Perkins b, I. Walter d

Müllerová J., Pergl J. and Pysek P. Remote sensing as a tool for monitoring plant invasions: Testing the effects of data resolution and image classification approach on the detection of a model plant species *Heracleum mantegazzianum* (giant hogweed). *International Journal of Applied Earth Observation and Geoinformation*. **2013**, 25, 55–65.

Müllerová, J.; Brůna, J.; Dvořák, P.; Bartaloš, T.; Vítková, M. Does the data resolution/origin matter? Satellite, airborne and UAV imagery to tacle plant invasions. *The International Archives of the Photogrammetry, Remote Sensing and Spatial Information Sciences*, **2016**, XLI-B7, 903-908.

Müllerová, J.; Bartaloš, T.; Brůna, J.; Dvořák, P.; Vítková, M. Unmanned aircraft in nature conservation: an example from plant invasions. *International Journal of Remote Sensing*.**2017**, 38(8-10), 2177-2198.

Mzezwa, J.; Mlisi, T.; van Rensburg, L. Characterisation of rainfall at a semi-arid ecotope in the Limpopo province (South Africa) and its implications for sustainable crop production. *Water SA*, **2010**, 36(1), 19-26.

Ngubane, Z.; Odindi, J.; Mutanga, O.; Slotow, R. Assessment of the contribution of WorldView-2 strategically positioned bands in Bracken fern (*Pteridium aquilinum* (L.) Kuhn) mapping. South African Journal of Geomatics. **2013**, 3(2), 210-223.

Nguyen, H.C.; Jung, J.; Lee, J.; Choi, S.U.; Hong, S.Y.; Heo, J. Optimal atmospheric correction for above-ground forest biomass estimation with the ETM+ remote sensor. *Sensors*. **2015**, 15, 18865–18886.

Novoa, A.;Le Roux, J. J.; Robertson, M. P.; Wilson, J.R.U.; Richardson, D.M. Introduced and invasive cactus species: a global review. **2015**, *AoB PLANTS 7*, plu078.

Osborne, M. Arduplot Mission planner. Available online: http://planner.ardupilot.com/ (Accessed on 10 August **2016**).

Pádua, L.; Vanko, J.; Hruška, J.;Adão, T.;Sousa, J.J.; Peres, E.;Morais, R. UAS, sensors, and data processing in agroforestry: a review towards practical applications. *International Journal of Remote Sensing*.**2017**, 38(8-10), 2349-2391.

Peerbhay, K.; Mutanga, O.; Ismail, R. The identification and remote detection of alien invasive plants in commercial forests: An overview. South African Journal of Geomatics.**2016**, 5(1), 49-67.

Poona N. K. and Shezi I. Z. An investigation into using different satellite remote sensors and techniques to identify, map, monitor and predict the spread and distribution of some of the major current and emerging invasive alien plant species in KwaZulu-Natal. Invasive Alien Species Programme (DEAA). 2010, 1-105.

Primicerio, J.; Di Gennaro, S. F.; Fiorillo, E.; Genesio, L.; Lugato, E.; Matese A.; Vaccari, F. P. A flexible unmanned aerial vehicle for precision agriculture. *Precision Agric*. **2012**, 13(4), 517-523.

Rao, R. N. Development of a crop-specific spectral library and discrimination of various agricultural crop varieties using hyperspectral imagery. *International Journal of Remote Sensing*.**2008**, 29(1), 131-144.

Richardson, D.M., van Wilgen, B.W.Invasive alien plants in South Africa: How well do we understand the ecological impacts? *South Africa J. Sci.* **2004**, 100, 45–52.

Rinaudo, F.; Chiabrando, F.; Lingua, A.; Spano, A. Archeological site monitoring: UAV photogrammetry can be an answer. *The International Archives of the Photogrammetry, Remote Sensing and Spatial Information Sciences*. **2012**, XXXXIX-B5, 583-588.

Rokhmana, C.K. The potential of UAV-based remote sensing for supporting precision agriculture in Indonesia. *Procedia Environmental Sciences*. **2015**, 24, 245-253.

Sankey, T. T.; McVay, J; Swetnam, T. L.;McClaran, M.P.; Heilman, P.; Nichols, M. UAV hyperspectral and lidar data and their fusion for arid and semi-arid land vegetation monitoring. *Remote Sensing in Ecology and Conservation*.**2015**:1-14.

Samiappan, S.; Turnage, G.; Hathcock, L.A. Moorhead, R.Mapping of invasive phragmites (common reed) in Gulf of Mexico coastal wetlands using multispectral imagery and small unmanned aerial systems. *International Journal of Remote Sensing*.**2017,** 38(8-10):2861-2882

Schloderer, G.; Bingham, M.; Awange, J.L.; Fleming, K. M. Applications of GNSS-RTK derived topographical maps for rapid environmental monitoring: a case study of Jack Finney Lake (Perth, Australia). *Environ Monit Assess*, **2010**, 180(1-40,147-161.

Sebari, I., He, D.C., 2013. Automatic fuzzy object-based analysis of VHSR images for urban objects extraction. *ISPRS J. Photogramm. Remote Sens.***2013**, 79,171–184.

Senseman, G. M.; Bagley, C. F.; Tweddale, S. A. Accuracy assessment of the discrete classification of remotely-sensed digital data for land-cover mapping. USACERL Technical Report EN-95/04. U. S. Army Corps of Engineers, Champaign,IL, **1995**, 1-27

Silva, A. F.; Barbosa, P. A.; Zimback, C. R. L.; Landim P. M. B. Geostatistics and remote sensing methods in the classification of images of areas cultivated with citrus'. Engineering Agriculture.**2013**, 33(6), 1245-1256.

Smith, G.M.; Milton, E.J. The use of the empirical line method to calibrate remotely sensed data to reflectance. *International Journal of Remote Sensing.***1999**, *20*(13), 2653-2662.

Sonaa, G.; Passonia, D.; Pintoa, L.; Pagliaria, D.; Masseroni, D.;Ortuanib, B.; Facchib, A. UAV multispectral survey to map soil and crop for precision farming applications. *The International Archives of the Photogrammetry, Remote Sensing and Spatial Information Sciences.* **2016**, XLI-B1:1023-1029.

Tesfamichael, S. G.;Newete, S. W.; Adamd, E.; Dubula, B. Field spectroradiometer and simulated multispectral bands for discriminating invasive species from morphologically similar cohabitant plants. *GIScience & Remote Sensing*. **2017**: 1548-1603.

Thiel, C.; Schmullius, C. Comparison of UAV photograph-based and airborne lidar-based point clouds over forest from a forestry application perspective. *International Journal of Remote Sensing.* **2017**, 38(8-10): 2411-2426.

Torrescan, C.; Berton, A.; Carotenuto, F.; Di Gennaro, S. F.; Gioli, B.; Matese, A.; Miglietta, F.; Vagnoli, C.; Zaldei, A.; Wallace, L. Forestry applications of UAVs in Europe: a review. *International Journal of Remote Sensing*, 2017, 38(8-10), 2427-2447.

Tuanmu, M.; Vina, A., Bearer, S., Xu, W., Ouyang, Z., Zhang, H., Liu, J. Mapping understory vegetation using phenological characteristics derived from remotely sensed data. *Remote Sens. Environ*, **2010**, 114, 1833-1844.

Underwood, E.; Ustin, S.; Di Pietro, D. Mapping non-native plants using hyperspectral imagery. *Remote Sens. Environ*. **2003**, 86, 150-161.

Underwood, E. Ustin, S.L., Ramirez, C. (2006a) A comparison of spatial and spectral image resolution for mapping invasive plants in coastal California. *Environmental Management*, 2006a, 39: 63-83.

Underwood, E., Mulitsch, M.J., Greenberg, J.A., Whiting, M.L., Ustin, S.L., Kefauver, S.C. Mapping invasive aquatic vegetation in the Sacramento-San Joaquin Delta using hyperspectral imagery. *Environmental Monitoring and Assessment*, 2006b, 121: 47-64.

Ustin, S.L., Santos, M.J.,. Spectral identification of native and non-native plant species. In: Proceedings of ASD and IEEE GRS; Art, Science and Applications of Reflectance Spectroscopy Symposium, vol. II, Boulder, Colorado, February 23–25, **2010**, 17

Van Wilgen B. W. The evolution of fire and invasive alien plant management practices in fynbos. *S. Afri. J. Sci*. **2009**, 105, 9,335-342.

Vilà, M.; Espinar, J.L.; Hejda, M.; Hulme, P.E.; Jarošík, V.; Maron, J.L.; Pergl, J.; Schaffner, U.; Sun, Y.; Pyšek, P. (2011) Ecological impacts of invasive alien plants: a meta-analysis of their effects on species, communities and ecosystems. *Ecol. Lett.* **2011**, 14, 702-708.

Wan, H.; Wang, Q.; Jiang, D.; Fu, J.; Yang, Y.; Liu, X.Monitoring the Invasion of Spartina alterniflora Using Very High Resolution Unmanned Aerial Vehicle Imagery in Beihai, Guangxi (China). *The Scientific World Journal*.**2014**, 1-7.

Wang, C.; Myint, S.W. A simplified empirical line method of radiometric calibration for small unmanned aircraft systems-based remote sensing. IEEE J-STARS **2015**, 8, 1–10.

Wang, L.; Zhang, Y.; Feng, J. On the euclidean distance of images. *IEEE Transactions on Pattern Analysis and Machine Intelligence*. **2005**, 27(8), 1334–1339.

Wang, L.; Silván-Cárdenas, J L.; Yang, J.;Frazier, A. E.Invasive Saltcedar (*Tamarisk spp.)* Distribution Mapping Using Multiresolution Remote Sensing Imagery. *The Professional Geographer*.**2013**, 65:1, 1-15

Wang, T.; Skidmore, A.; Toxopeus, A. Improved understorey bamboo cover mapping using a novel hybrid neural network and expert system. Int. J. Remote Sens.**2009**, 30(4), 965-981.

Wang, Q.; Wu, L.; Chen, S.; Shu, D.; Xu, Z.; Li F.; Wang, R. Accuracy evaluation of 3D geometry from low-attitude UAV images: A case study at Zijin mine. *ISPRS – Archives*. **2014**, XL-4, 297-300.

Wiechert, A.; Gruber, M.; Ponticelli, M. Ultracam: The new super-large format digital aerial camera. ASPRS 2011 Annual Conference, Milwaukee, Wisconsin, May1-5, **2011**.

Williams, P. A. E.; Hunt, E.R. Accuracy assessment for detection of leafy spurge with hyperspectral imagery. *Journal of Range Management*, **2004**, 57: 106-112.

Wilson J.R.; Ivey P.; Manyama P.; Nanni I. A new national unit for invasive species detection, assessment and eradication planning. *S. Afri. J. Sci.* **2013**, 109, 5, 61-13.

Yang C., Everitt J. H. And Murden, D. Evaluating high resolution STOP 5 satellite imagery for crop identification. *Computers and Electronics in Agriculture, Netherlands*. **2011,** 75,347-354.

Yang, G.; Liu, J.; Zhao, C.; Li, Z.; Haung, Y.; Yu, H.; Xu, B.; Yang, X.; Zhu, D.; Zhang, X.; Zhang, R.; Feng, H.; Zhao, Z.; Li, Z.; Li, H.; Yang, H. Unmanned aerial vehicle remote sensing for field-based crop phenotyping: current status and perspectives. *Front. Plant Sci*.**2017**, 8:1111.

Zhang, Z. X. **2014**. Native vegetation classification using remote sensing techniques: A case study of dairy flat regrowth bush by using the AUT unmanned aerial vehicle. Master of Science. Auckland University of Technology. New Zealand.